



**HAL**  
open science

## Aqueous Alteration as an Origin of Martian Magnetization

B. Bultel, M. Wieczorek, Anna Mittelholz, Catherine Johnson, Jérôme Gattacceca, Valentin Fortier, Benoit Langlais

► **To cite this version:**

B. Bultel, M. Wieczorek, Anna Mittelholz, Catherine Johnson, Jérôme Gattacceca, et al.. Aqueous Alteration as an Origin of Martian Magnetization. *Journal of Geophysical Research. Planets*, 2025, 130 (1), 10.1029/2023JE008111 . hal-04919008

**HAL Id: hal-04919008**

**<https://hal.science/hal-04919008v1>**

Submitted on 30 Jan 2025

**HAL** is a multi-disciplinary open access archive for the deposit and dissemination of scientific research documents, whether they are published or not. The documents may come from teaching and research institutions in France or abroad, or from public or private research centers.







L'archive ouverte pluridisciplinaire **HAL**, est destinée au dépôt et à la diffusion de documents scientifiques de niveau recherche, publiés ou non, émanant des établissements d'enseignement et de recherche français ou étrangers, des laboratoires publics ou privés.



Distributed under a Creative Commons Attribution - NonCommercial - NoDerivatives 4.0  
International License



## Aqueous Alteration as an Origin of Martian Magnetization

B. Bultel<sup>1</sup> , M. Wieczorek<sup>2</sup> , Anna Mittelholz<sup>3</sup> , Catherine L. Johnson<sup>4,5</sup> , Jérôme Gattacceca<sup>6</sup> , Valentin Fortier<sup>7,8,9</sup>, and Benoit Langlais<sup>10</sup> 

### Key Points:

- We determine the amount of magnetite necessary to account for the observed magnetic field strengths
- We model the minerals that are produced by serpentinization of the martian crust
- Aqueous alteration of dunites at low water-to-rock ratios can generate sufficient magnetite to account for the strongest magnetic anomalies

<sup>1</sup>GEOPS, Université Paris-Saclay, CNRS, Orsay, France, <sup>2</sup>Institut de Physique du Globe de Paris, Université Paris Cité, CNRS, Paris, France, <sup>3</sup>Department of Earth and Planetary Sciences, ETH Zurich, Zurich, Switzerland, <sup>4</sup>University of British Columbia, Vancouver, BC, Canada, <sup>5</sup>Planetary Science Institute, Tucson, AZ, USA, <sup>6</sup>Aix-Marseille Univ, CNRS, IRD, INRAE, CEREGE, Aix-en-Provence, France, <sup>7</sup>Université Catholique de Louvain-la-Neuve, Earth and Life Institute, Louvain-la-Neuve, Belgium, <sup>8</sup>Laboratoire G-Time, Université Libre de Bruxelles, Bruxelles, Belgium, <sup>9</sup>Géosciences Montpellier, CNRS, Univ. Montpellier, Montpellier, France, <sup>10</sup>Laboratoire de Planétologie et Géosciences UMR 6112, Nantes Université, Univ Angers, Le Mans Université, CNRS, Nantes, France

### Supporting Information:

Supporting Information may be found in the online version of this article.

### Correspondence to:

B. Bultel,  
benjamin.bultel@universite-paris-saclay.fr

### Citation:

Bultel, B., Wieczorek, M., Mittelholz, A., Johnson, C. L., Gattacceca, J., Fortier, V., & Langlais, B. (2025). Aqueous alteration as an origin of Martian magnetization. *Journal of Geophysical Research: Planets*, 129, e2023JE008111. <https://doi.org/10.1029/2023JE008111>

Received 3 OCT 2023  
Accepted 20 NOV 2024

**Abstract** Strong magnetic fields have been measured from orbit around Mars over parts of the ancient southern highlands crust and on the surface at the InSight landing site. The geological processes that are responsible for generating strong magnetization within the crust remain poorly understood. One possibility is that intense aqueous alteration of crustal materials, through the process of serpentinization, could have produced magnetite that was magnetized in the presence of a global core-generated magnetic field. Here, we test this idea with geophysical and geochemical models. We first determine the magnetizations required to account for the observed magnetic field strengths and then estimate the amount of magnetite necessary to account for these magnetizations. For the strongest orbital magnetic field strengths, about 7 wt% magnetite is required if the magnetic layer is 10 km thick. For the surface field strength observed at the InSight landing site, 0.4–1.1 wt% magnetite is required if the magnetic layer corresponds to one or more of the three crustal layers observed in the InSight seismic data (with thicknesses from 8 to 39 km). We then investigate the minerals that are produced by aqueous alteration for various possible crustal compositions and water-to-rock ratios using a thermodynamic model. Magnetite abundances up to 6 wt% can be generated for dunitic compositions that could account for the strongest magnetic anomalies. For more representative basaltic starting compositions, however, more than 0.4 wt% can only be generated when using high water-to-rock ratios, which could account for the weaker magnetizations beneath the InSight landing site.

**Plain Language Summary** The core of Mars once generated a global magnetic field that magnetized portions of the crust. Locally, these magnetic anomalies are surprisingly strong, with field strengths about 10 times larger than those associated with remanent magnetization of the Earth's crust. The origin of the Martian magnetic anomalies has long been debated, and we investigate whether aqueous alteration of Martian rocks (by the process of serpentinization) can generate sufficient quantities of magnetite to account for orbital and surface magnetic field observations. We first show that the strongest magnetic anomalies detected from orbit can be accounted for by about 1–7 wt% magnetite in a layer that is more than 10 km thick, and that the measured surface field strength at the InSight lander can be accounted for by 0.4–1.1 wt% magnetite in a crustal layer that is more than 8 km thick. Aqueous alteration of dunites at low water-to-rock ratios can generate sufficient magnetite to account for the strongest magnetic anomalies, whereas aqueous alteration of shergottites and pyroxenites at higher water-to-rock ratios can account for the InSight measurements.

## 1. Introduction

Magnetic field observations from the orbiting Mars Global Surveyor and Mars Atmosphere and Volatile Evolution spacecraft (Acuña et al., 1999; Connerney, 2015; Langlais et al., 2010; Mittelholz et al., 2023) have shown that the planet Mars is surprisingly magnetic. While Mars does not possess a global dipolar magnetic field that is generated by its core today, portions of its crust are associated with strong magnetic fields that far exceed the lithospheric field strengths of Earth. Magnetic field observations vary globally with a mean field amplitude of 64 nT at 130 km altitude above the surface of Mars, but the strongest field strengths reach about 1,541 nT (Langlais et al., 2019). At the same altitude, terrestrial lithospheric field strengths are about 10 times weaker. The orbital observations are resolution limited by the lowest altitude data available (Mittelholz et al., 2023), and measurements of the magnetic field on the surface of Mars by the InSight lander were found to be higher than

© 2025. The Author(s).

This is an open access article under the terms of the [Creative Commons Attribution-NonCommercial-NoDerivs License](#), which permits use and distribution in any medium, provided the original work is properly cited, the use is non-commercial and no modifications or adaptations are made.

predicted using crustal magnetic field models. Surface measurements at the InSight landing site show a magnetic field amplitude of  $\sim 2,000$  nT, compared to 200–300 nT as predicted from models (Johnson et al., 2020; Smrekar et al., 2019).

Since the discovery of the strong Martian magnetic anomalies, numerous investigations have been undertaken to elucidate their origin, but there is little consensus. On the most fundamental level, the magnetic minerals responsible for these anomalies are not known with certainty. Magnetite, titanomagnetite, pyrrhotite, hematite, maghemite, and titanomagnetite have all been proposed, with single-domain pyrrhotite and magnetite being the most plausible candidates (e.g., Dunlop & Arkani-Hamed, 2005). Both pyrrhotite and magnetite are known to be present in the Martian meteorites (e.g., Rochette et al., 2005), but with rare exceptions, these meteorites are not representative of the bulk crust of Mars (cf., McSween & McLennan, 2014; Humayun et al., 2013). Even if the predominant magnetic mineral responsible for the Martian magnetic anomalies could be identified, there are several potential origins for these minerals, including primary minerals that formed during magmatic processes, impactor contamination in impact deposits such as on the Moon (Oliveira et al., 2017; Wieczorek et al., 2012), and the formation of new magnetic minerals during aqueous alteration of crustal materials. It is the last of these hypotheses that will be addressed in this work.

Hydration of the Martian crust was first advocated by Quesnel et al. (2009) as a means to generate large quantities of magnetite that could perhaps account for the strong magnetic anomalies observed from the orbit. Serpentinization is a process where mafic silicates (olivine and pyroxene) react with water, leading to the formation of magnetite and hydrous minerals such as serpentine and brucite. If an ambient magnetic field were present when the alteration was occurring, the magnetite that was produced could retain a remanent magnetization through a process known as chemical remanent magnetization (see chapter 13, Dunlop & Özdemir, 1997). As surface materials on Mars are composed primarily of mafic basalts that contain high quantities of olivine and pyroxene, serpentine formation is an appealing process for explaining the Martian magnetic anomalies (although the process would be more limited than in more mafic rocks such as dunite). This process could potentially represent an important sink of water in the crust, and the methane and  $H_2$  gases that are produced as reaction by-products (e.g., Chassefière et al., 2013; Chassefière & Leblanc, 2011) could help to account for the greenhouse conditions responsible for early clement conditions on the planet (e.g., Ramirez et al., 2020; Turbet, 2018). Furthermore, an overall correlation between surface runoff in valley networks and magnetic anomalies has been observed (Harrison & Grimm, 2002). The InSight mission has shown that the upper 10 km of the crust beneath the lander has extremely low seismic velocities, and one interpretation of this observation is that these materials represent aqueously altered materials (Lognonné et al., 2020).

In the early work of Quesnel et al. (2009) and Chassefière & Leblanc, 2011, simplified chemical reactions were used to estimate the possible amounts of magnetite that could be produced by serpentinization. Their models, however, were developed for the alteration of a more mafic crust with a composition close to that of dunite and pyroxenite. These compositions are not representative of the bulk Martian crust, which is likely to be more felsic than the basaltic shergottites (e.g., Wieczorek et al., 2022). Furthermore, neither of these studies used a thermodynamic model to properly define the conditions needed for the proposed chemical reaction to occur. In addition to the composition of the host rock, other important parameters that influence magnetite production, and that were not previously considered, are temperature and the magnesium number (hereafter, Mg#) of olivines and pyroxenes (see Klein et al., 2014; Evans, 2008, respectively). The Mg# corresponds here to the molar percent of the Mg-endmember mineral part of the solid solution considered (olivine with an Mg# of 90 corresponds to a solid solution of 90 mol% forsterite and 10 mol% fayalite). Low-temperature serpentinization (less than about  $180^\circ\text{C}$ ) is known to generally favor the formation of  $\text{Fe}^{3+}$ -serpentine rather than magnetite as well as the formation of Fe-brucite rather than Mg-brucite (Klein et al., 2014). In addition, Martian olivines and pyroxenes are expected to be more iron-rich than their Earth counterparts, which could potentially affect the amount of magnetite that is produced. This was studied by geochemical models in McCollom et al. (2022), which shows that for an Mg# of 100 to  $\sim 70$ –60, the amount of magnetite increases while it decreases for lower Mg#. It is also likely that the alteration would lead to some amount of substitution of Fe by Cr or Ti into the produced magnetite, and this could affect the overall magnetic properties of the magnetic minerals (e.g., Dunlop & Özdemir, 2015; O'Reilly, 1984).

These considerations suggest that the efficiency of magnetite production by aqueous alteration might have been overestimated in previous studies, and this compels us to re-evaluate whether aqueous alteration could generate enough magnetite to account for the Martian magnetic anomalies. In this study, we first reassess how much

magnetite is required to account for the strongest magnetic anomalies observed from the orbit and the magnetic field strength measured at the InSight landing site. We then use a thermodynamic code to estimate how much magnetite can be produced by aqueous alteration of Martian rocks, using compositions that range from ultramafic to felsic. In addition to investigating the effects of bulk rock composition and magnesium number, we also assessed the influence of temperature and the water-to-rock ratio on magnetite production.

The remainder of this paper is organized as follows. First, we describe our approach for determining the magnetization that is required to account for a given magnetic anomaly, and how we determine the associated abundance of magnetite from these estimates. In the same section, we then describe how the thermodynamic code EQ3/6 (Wolery, 2010; Wolery et al., 1990) is used to model the aqueous alteration of crustal rocks and discuss the rock compositions that will be investigated. Next, in Section 3, by focusing on both the strongest magnetic anomaly detected from orbit and the field strength at the InSight lander, we estimate the required magnetizations and abundances of magnetite within the crust. In Section 4, we present our aqueous alteration results, highlighting the factors that influence the efficiency of magnetite production. Lastly, in Section 5 we discuss several aspects of our work, including how our results compare with the magnetic properties of Martian meteorites and rocks, whether aqueous alteration could be responsible for Martian magnetization, and how our simulated alteration products compare with aqueous alteration signatures detected from orbit in remote sensing data.

## 2. Methods

### 2.1. Crustal Magnetization

It is possible to estimate how the magnitude and direction of magnetization vary within the crust by using magnetic field measurements. Such inversions, however, are inherently non-unique, and it is necessary to make simplifying assumptions to arrive at a solution. One approach developed by Parker (2003) allows estimating a minimum value of the magnetization within the crust by use of a single magnetic field measurement. This approach is mathematically “ideal” in that the directions of magnetization in the surrounding crust are chosen to maximize the magnetic field strength at the measurement location. The benefit of this approach is that only a single measurement is required and the only free parameters in the model are the thickness of the magnetic layer and the depth of this layer below the surface of the planet. The downside is that the assumed magnetization directions are not geologically plausible: a core-generated magnetic field would be approximately unidirectional in the vicinity of the analysis region. When the magnetic field is known either regionally or globally, it becomes possible to invert for variations in the direction and magnitude of magnetization within the crust. With these approaches, however, one generally needs to assume the thickness of the magnetic layer and apply a regularization constraint (e.g., Butler, 1998; Langlais et al., 2019; Lesur & Vervelidou, 2019; Parker, 1991; Thébaud et al., 2021, and references therein).

To obtain bounds on the magnitude of magnetization within the crust of Mars, we make use of a model that is likely to be appropriate for many geologic processes. We assume that the crust is regionally non-magnetic except for a single compact source that has a constant magnitude and direction of magnetization. For simplicity, the compact source is here taken to be a thick spherical cap that is described by its angular radius, the depth to the top of the cap, and the cap thickness. Such a geometry could correspond to a surface lava flow, an impact crater melt sheet, or a magmatic intrusion. For a given depth and thickness, we then vary the cap radius to determine the minimum magnetization that can account for a specified value of the magnetic field strength at a specified height above the surface.

In practice, we first compute the spherical harmonic coefficients of a magnetized thick spherical cap using the equations in Wicczorek (2018) for the case where the magnetization is set equal to  $1 \text{ Am}^{-1}$ . Since we are interested in obtaining the minimum magnetization, we assume that the direction of magnetization is vertical. For a given set of parameters, the maximum value of the predicted magnetic field intensity is computed at the altitude of the magnetic field measurement, and the initial magnetization is then rescaled to match the observed field strength. Repeating this process for a range of angular radii of the magnetized body (from just greater than 0 to several hundred km) allows us to determine the minimum required magnetization. This model with compact sources is likely to provide a more realistic minimum value for the magnetization than the idealized approach developed by Parker (2003).

## 2.2. Abundance of Magnetic Minerals From Magnetization

The conversion from a rock's magnetization to the abundance of magnetic minerals in the rock requires making several assumptions, including the predominant magnetic species that is responsible for the magnetization, the intrinsic magnetic properties of these minerals, and the ambient magnetic field when the rock was magnetized. Here, we assume that only a single magnetic species is present in the crust and that all magnetic minerals were magnetized in a steady ambient magnetic field. For this scenario, Oliveira et al. (2017) showed that the volume fraction of the magnetic mineral,  $c$ , could be obtained using the equation

$$c = \frac{a}{sBM_s^\dagger} M_r \quad (1)$$

Here,  $a$  is an empirical constant that quantifies the efficiency of magnetizing a rock in a specified magnetic field, which depends upon the magnetization process and the magnetic mineral and domain state. The quantity  $s$  represents the ratio of the rock saturation remanent magnetization  $M_{rs}$  and rock saturation magnetization  $M_s$  that can both be measured in the laboratory, and that largely reflects the domain state of the magnetic minerals.  $B$  is the strength of the ambient magnetic field when the remanent magnetization  $M_r$  was acquired. Lastly,  $M_s^\dagger$  is the saturation magnetization of the magnetic mineral. The volume% of the magnetic carrier can be converted to weight% by assuming densities of the magnetic mineral and silicates.

By using the derived crustal magnetization for  $M_r$  as described in the previous subsection, it is possible to estimate the concentration of magnetic minerals in the magnetic layer if the other constants in Equation 1 are known. The constant  $a$  has been determined empirically for the case of chemical remanent magnetization by Maurel and Gattacceca (2023), and we use their log-normal average of 3,629  $\mu\text{T}$  that has a multiplicative uncertainty of a factor of 1.9. We note that chemical remanent magnetization is less efficient than thermoremanent magnetization by a factor of almost two, and that the required magnetic mineral abundances are thus about two times larger than for the case of thermoremanent magnetization. In particular, the log-normal average of single- and pseudo-single domain magnetite samples tabulated in Weiss and Tikoo (2014) for thermoremanent magnetization is 1,470  $\mu\text{T}$ .

For the ratio,  $s$ , we make use of 33 measurements of Martian meteorites tabulated in Rochette et al. (2005), Gattacceca et al. (2014), Herd et al. (2017), and Krämer Ruggiu et al. (2020), along with 13 new measurements presented in Table S4 in Supporting Information S1. The average  $s$  for these meteorites is 0.28, with the individual meteorites possessing a limited range from 0.11 to 0.49. These values indicate that the magnetic minerals are predominantly in the single- to pseudo-single domain states. By using the  $S_{300}$  ratio to discriminate between meteorites that are dominated by magnetite or pyrrhotite (see Appendix A in Supporting Information S1), we find that the magnetic mineralogy of these rocks has little influence on the value of  $s$  ( $s$  is respectively 0.26 and 0.34).

Based on the results of our aqueous alteration simulations that will be discussed in the following section, we assume that magnetite is the predominant magnetic mineral responsible for the remanent magnetic fields observed from orbit and on the surface of Mars. The saturation magnetization of magnetite,  $M_s^\dagger$ , is known to be  $4.8 \times 10^5 \text{ A m}^{-1}$  (e.g., Dunlop & Özdemir, 2015). Nevertheless, we acknowledge that both pyrrhotite and titanomagnetite are known to be important magnetic minerals for many of the Martian meteorites. In particular, whereas (titano)magnetite is generally the predominant magnetic mineral for the nakhlites, chassignites, and NWA 7034 (and its pairs), pyrrhotite is the predominant phase for most of the basaltic meteorites, though there are many exceptions to this rule (e.g., Gattacceca et al., 2014; Rochette et al., 2005). The saturation magnetization of titanomagnetite and pyrrhotite are respectively 4 and 5 times lower than for pure magnetite (e.g., Dunlop & Özdemir, 2015), and to obtain the same rock magnetization, it would thus be necessary to have 4 to 5 times higher concentrations of these minerals. Nevertheless, it should be noted that both titanomagnetite and pyrrhotite have significantly lower Curie temperatures than magnetite (respectively 150 and 320°C, in contrast to 580°C for magnetite) and that this places restrictive limits on the depth range in the crust where they could retain a remanent magnetization (Dunlop & Arkani-Hamed, 2005). The magnetic mineral maghemite, which is present in the NWA 7034 meteorite, has a saturation magnetization and Curie temperature that are close to those of magnetite. However, maghemite often transforms to hematite at low temperatures of 250–550°C, losing most of its initial magnetization in the process (Dunlop & Özdemir, 2015).



The last value that is required in Equation 1 is the magnetizing field strength  $B$ . This has been constrained by analyses of the ancient ALH84001 meteorite by Weiss et al. (2008), who obtained a value of  $46 \mu\text{T}$  using the isothermal technique of normalizing the natural remanent magnetization by the saturation isothermal remanent magnetization. Nevertheless, they noted that subsamples of this rock gave paleo-field strengths that varied by about a factor of 6. Lacking better knowledge of the surface field strength and how it might have varied with time, we assume a value of  $50 \mu\text{T}$ .

### 2.3. Water-Rock Interaction Modeling

Our aqueous alteration simulations were performed using the software code EQ3/6 (version 8.0, Wolery et al., 1990). We make use of a customized database for the temperature range  $0\text{--}300^\circ\text{C}$  that was initially used by Viennet et al. (2017) and that proved itself reliable in reproducing hydrothermal conditions (Appendix B in Supporting Information S1). To allow studying the water-rock interaction in detail, and to allow investigation of our initial protolith compositions, we added a few solid solutions constructed from the pure endmembers in this thermodynamic database (see Table S3 in Supporting Information S1 for more details on the mineral compositions). Most of these concerns oxides. In particular, we included four iron oxide solid solutions formed of chromite and magnesiochromite, magnetite and ulvospinel, spinel and hercynite, and hematite and ilmenite. A solid solution of the hydroxide brucite with both its iron and magnesium endmembers was also implemented. An additional solid solution was used for the phyllosilicate serpentine with the Al endmember kaolinite, the  $\text{Fe}^{3+}$  endmember cronstedtite, the  $\text{Fe}^{2+}$  endmember greenalite, and the Mg endmember chrysotile. Note that to discuss the water-rock interactions and formation of magnetite, all solid solutions of iron (hydro-)oxide are investigated and are described in the results section.

For all models, the fluid was initially specified by using the code EQ3 with a temperature of  $25^\circ\text{C}$ . We conducted two kinds of models, one with pure water of neutral pH and one with a simulated Martian water composition from Catling (1999) in equilibrium with 1 bar of  $\text{CO}_2$ . The code EQ6 was then used to simulate the alteration using a water-to-rock ratio of 1, 10, 100 or 1000. A water-to-rock ratio of 1 is typically taken as being representative for the conditions where water flows through a fracture in a rock (see Seyfried & Bischoff, 1977, 1979, 1981). A “pure water-neutral pH” solution was used for this low water to rock ratio. Our hypothesis here is that the water was not in contact with the atmosphere and did not interact with any rock before. For low water-to-rock ratios ( $<10$ ), the initial solution composition should not have an important influence on the reaction and this hypothesis should thus not affect the simulation outcome. In this case, it is the composition of the rock that controls the alteration products that are formed. In contrast, a water-to-rock ratio of 10 or more is typically taken to represent the conditions of alteration that occur in porous rock, in an aquifer, or at the interface between a standing body of water and the surface. In these high water to rock systems, we hypothesize that the water could have previously interacted with both rocks and the atmosphere before the model reactions took place. That is why for these high water to rock models we use the water composition of Catling (1999). Nevertheless, in the case of a water-to-rock ratio of 10, the effect of the initial composition of the water on final alteration products is limited. For water-to-rock ratios much greater than 100, the system would be completely dominated by the water composition. We note that the effective water-to-rock ratio of a system can be increased by either increasing the rock porosity, by increasing the time of the interaction, or by lowering the rock permeability (see Lyons et al., 2005). As an example, using typical values in the equations of Lyons et al. (2005), we find that increasing the interaction time from 1000 to 100,000 years increases the effective water-to-rock ratio from about 100 to  $10^6$ .

The next step of the simulation includes heating of the aqueous solution to the desired temperature in the EQ6 code. Two temperatures were chosen ( $100^\circ\text{C}$  and  $200^\circ\text{C}$ ) to study the alteration of both olivine and pyroxene and to quantify how temperature affects the formation of magnetite. As estimates of the temperature gradient during the Noachian and Hesperian periods are between 20 and  $30 \text{ K km}^{-1}$ , these temperatures would be encountered in the upper 10 km of the crust when the Martian dynamo was operating (Hauck & Phillips, 2002). Finally, we model the interaction between the heated solution and the rock using the EQ6 code. A reaction path is applied with the “reaction progress mode,” and the progress of the reaction is visualized by using the percentage of the dissolved rocks. We applied an arbitrary kinetics in a closed system. This means that all processes are constrained by relative rate expressions and that no time variable is at play in the model (see Wolery & Jarek, 2003 for more details). In all of our models, backward reactions (such as the dissolution of the product) are permissible, as is the formation of solid solutions. We suppress the formation of methane and methanol as these reactions are

kinetically slow and not well tested, and also vermiculite because it should form mainly from mica, which is not present in the protoliths used here (Barshad, 1948). The formation of monticellite and garnet (when not present in the starting material) is also suppressed because they should not form in the geological context we investigate. When we do allow for their formation, we note that they are only present in trace quantities (<0.1 wt%) and absent at the end of the reaction (100% dissolution of the protolith). Throughout this paper, we use the term “trace” to describe mineral abundance below 2 wt%, which is below the detection limit of many analytical techniques commonly used, including X-ray diffraction and Near-Infrared spectroscopy.

#### 2.4. Initial Rock Compositions

We consider a wide range of initial rock compositions that could potentially be found within the crust of Mars. The compositions are presented in Table S1 in Supporting Information S1 and here we discuss their most relevant features. Our first suite of rocks focuses on ultramafic compositions with high olivine contents, i.e., dunites. Three values for the magnesium number of the olivine were used to represent a range of plausible compositions. First, we use an Mg# of 90, which is representative of typical mantle olivine on Earth (McDonough & Sun, 1995), but also consider lower magnesium numbers of 75 and 79 that are based on the bulk Mars compositions of Wänke and Dreibus (1994) and Yoshizaki and McDonough (2020), respectively. This range encompasses the average magnesium numbers of Martian meteorites and orbital remote sensing results (Ikeda, 1994; McSween & Lauretta, 2006; Ody et al., 2012) as well as a recent geophysical estimate from InSight seismic data (Khan et al., 2022). We assume that the dunite is composed of 90 wt% olivine and includes 2.5 wt% each of low calcium pyroxene (Mg# 75), high calcium pyroxene (Mg# 75), plagioclase (60 wt% albite) and chromite, which are typical accessory minerals of such rocks.

We next consider a mafic pyroxenite with a composition that is based on data in Treiman (2005) for nakhlite meteorites. This protolith contains 44.6 wt% low calcium pyroxene (Mg# 58), 29 wt% high calcium pyroxene (Mg# 58), 17 wt% olivine (Mg# 75), 6.8 wt% plagioclase (66 wt% albite), 0.75 wt% K-feldspar and 0.3 wt% chromite. This protolith composition allows us to study the alteration of a pyroxene-dominated system and to compare our results with the alteration seen in nakhlite meteorites where both magnetic minerals and serpentine are present (Changela & Bridges, 2010; Hicks et al., 2014).

We also consider an ultramafic composition that is representative of the upper Martian mantle. Several mantle compositions have been suggested in the literature, and we select one that is described in Semprich et al. (2022) that has a fluid-rich mantle. This composition will later be referred to as “Mantle-garnet” and is composed of 55.9 wt% olivine (Mg# 75), 27.3 wt% low calcium pyroxene (Mg# 75), 12.6 wt% high calcium pyroxene (Mg# 55), 3.8 wt% garnet (50 wt% andradite-50 wt% grossular), and 0.8 wt% spinel.

Finally, we consider both mafic and felsic rock compositions that are likely common in the crust of Mars. For the mafic compositions, we consider a basaltic rock with a shergottite lithology. This protolith is composed of 34.5 wt% high calcium pyroxene (Mg# 60), 27 wt% olivine (Mg# 66), 22 wt% low calcium pyroxene (Mg# 60), 15.5 wt% plagioclase (65 wt% albite), and 1 wt% chromite. The more felsic composition is representative of some of the felsic rocks analyzed by the Curiosity rover in Gale crater (e.g., Sautter et al., 2015), as well as some of the felsic clasts within the Martian breccia meteorite NWA 7034 and its pairs (e.g., Humayun et al., 2013; Santos et al., 2015). In particular, we used a trachyte protolith with 54.6 wt% plagioclase (95.4 wt% albite), 22.9 wt% K-feldspar, 10 wt% quartz, 7.6 wt% low calcium pyroxene (Mg# 60), 4 wt% diopside and 1 wt% ilmenite.

### 3. Crustal Magnetization Results

#### 3.1. Strongest Orbital Magnetic Anomaly

We first determined the magnetization that is required to account for the strongest magnetic fields measured from the orbit using the methodology outlined in Section 2.1. The strongest fields are located above the southern highlands of Mars in the region of Terra Cimmeria and Terra Sirenum, where we compute a maximum field strength of 1,197 nT at an altitude of 150 km above the mean planetary radius using the spherical harmonic model of Langlais et al. (2019).

In Figure 1, we show the minimum required magnetization to account for this field strength as a function of the thickness of the magnetic materials for two scenarios.

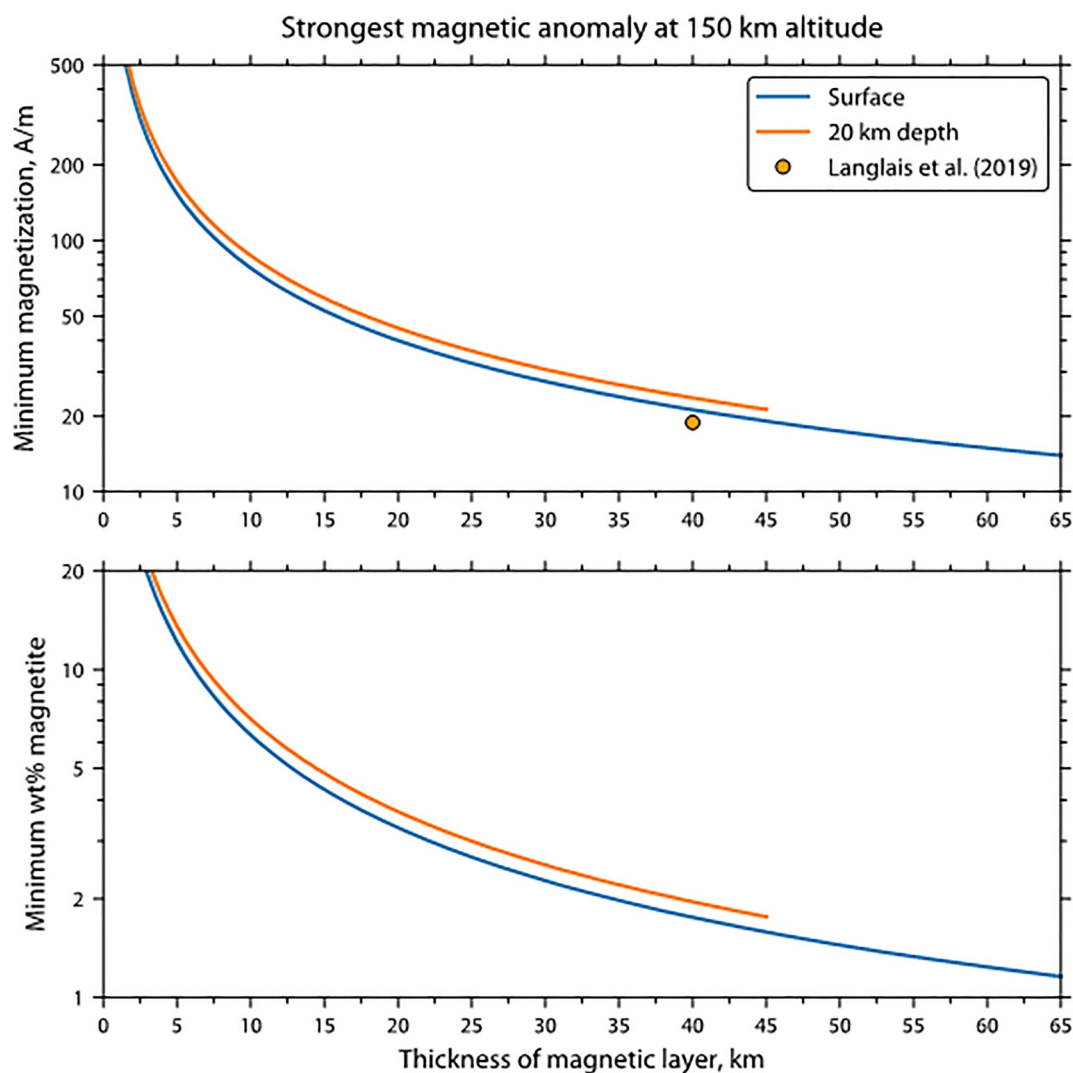


**Figure 1.** The minimum magnetization (top) and minimum abundance of magnetite (bottom) required to account for the strongest magnetic field strength,  $|B|$ , measured from orbit as a function of the thickness of the magnetized layer. Curves in blue and orange plot results where the top of the magnetic layer is at the mean planetary radius and at a depth of 20 km below the surface, respectively. The strongest field strength was taken from the global model of Langlais et al. (2019), which is 1,197 nT at an orbital altitude of 150 km. In the upper figure, the maximum magnetization from the global magnetization model of Langlais et al. (2019) is shown for comparison.

In the first scenario, the top of the compact magnetized spherical cap is placed at the mean planetary radius, and the thickness of the cap is allowed to vary up to a maximum of 65 km. For the second scenario, we placed the top of the spherical cap 20 km below the surface and allowed the base of the cap to vary up to the same maximum 65 km depth below the surface. The 20 km burial depth for the second scenario is based on the localized magnetic field spectral analysis study of Gong and Wiczeorek (2021), who showed that much of the magnetization in the southern highlands is located below this depth. The maximum depth of magnetization of 65 km that is used for both scenarios corresponds closely to the average thickness of the southern highlands crust in the constant-density crustal thickness model of Wiczeorek et al. (2022). Nevertheless, we note that magnetization is likely to be confined to shallower depths than this, as we don't expect hydrothermal alteration to occur this deep in the crust and the temperatures at this depth are likely to be above the Curie temperature of magnetite.

The assumed depth to the top of the magnetic materials has little impact on the computed magnetizations, which is a result of the spacecraft altitude being much greater than the assumed burial depth of the magnetic sources. As the thickness of the magnetized layer decreases, the required magnetization increases. As an example, for a thickness



**Table 1**

*Summary of Remanent Magnetizations, Saturation Remanent Magnetizations, and Concentrations of Magnetite Required to Account for the Strongest Orbital Magnetic Field Strength 150 km Above the Mean Planetary Radius and the Observed Field Strength at the InSight Lander*

| Magnetization scenario           | Magnetization ( $A m^{-1}$ ) | $M_{rs}$ ( $A m^{-1}$ ) | vol.% magnetite | wt% magnetite |
|----------------------------------|------------------------------|-------------------------|-----------------|---------------|
| Strongest orbital magnetic field |                              |                         |                 |               |
| 5 km thickness (20 km burial)    | 172                          | 5,063                   | 8.4             | 14            |
| 10 km thickness (20 km burial)   | 87                           | 2,568                   | 4.2             | 7.1           |
| 20 km thickness (20 km burial)   | 45                           | 1,320                   | 2.2             | 3.7           |
| 40 km thickness (20 km burial)   | 24                           | 696                     | 1.2             | 2.0           |
| InSight lander                   |                              |                         |                 |               |
| 0–8 km depth                     | 11                           | 323                     | 0.53            | 0.91          |
| 0–20 km depth                    | 5.9                          | 172                     | 0.29            | 0.49          |
| 0–39 km depth                    | 4.5                          | 130                     | 0.22            | 0.37          |
| 20–39 km depth                   | 14                           | 407                     | 0.67            | 1.1           |

*Note.* All values should be considered minimum values. If the magnetic mineral was in the form of titanomagnetite, the concentrations could be up to four times larger than quoted. The saturation remanent magnetization  $M_{rs}$  is estimated using an assumed magnetizing field strength of  $50 \mu T$ .

of 10 km, the required magnetization to account for the strongest magnetic anomaly is  $87 A m^{-1}$  for a 20 km burial depth. In contrast, when the thickness of the magnetized layer is 40 km, consistent with the results of Gong and Wieczorek (2021), the required magnetization is  $24 A m^{-1}$ . We note that our computed magnetizations compare favorably with the global magnetization model of Langlais et al. (2019), who obtained a maximum magnetization of  $19 A m^{-1}$  by assuming a 40 km thick magnetized layer. For a summary of these results and those that follow, see Table 1.

### 3.2. Insight Landing Site

Next, we performed the same calculations using the measured magnetic field strength at the InSight landing site, which is 2013 nT about 80 cm above the surface (Johnson et al., 2020). Analyses of the InSight seismic data show that the crust beneath the lander is broadly layered, with major discontinuities being located at 8, 20, and 39 km depth (the latter of which is interpreted as the crust-mantle interface). We thus consider three scenarios, where the top of the magnetization coincides with the top of each of these crustal layers. For the surface scenario, we assumed that the magnetization starts at 170 m depth to account for the presence of a reworked regolith, young sediments, and thin Amazonian to Early Hesperian lava flows (see Warner et al., 2022) that are likely unmagnetized.

The results in Figure 2 show that if the magnetization extended from 170 m to the base of the crust at 39 km depth, the minimum magnetization required to account for the surface field strength would be just over  $4 A m^{-1}$ . In contrast, if the magnetization was located only in the lowermost layer, between 20 and 39 km depth, the magnetization would need to be  $14 A m^{-1}$ . Using a localized magnetic field spectral analysis, Gong and Wieczorek (2021) showed that only the upper two layers of the northern lowlands crust are likely to magnetize, and our results imply that the minimum magnetization of these upper two layers would need to be about  $6 A m^{-1}$ .

We note that Johnson et al. (2020) previously used the Parker (2003) ideal body formalism for estimating the minimum magnetization in the crust beneath the InSight lander. As noted in Section 2, that model makes use of a geologically implausible ensemble of magnetization directions in the crust, and we find that the ideal body model thus predicts minimum magnetizations that are between 4 and 18 times less than those predicted by our model that uses compact unidirectionally magnetized sources.

### 3.3. Equivalent Abundances of Magnetite

In the lower panels of Figures 1 and 2, we plot the minimum abundances of magnetite that are required to account for the strongest magnetic anomaly observed from orbit and the observed field at the InSight lander. In converting

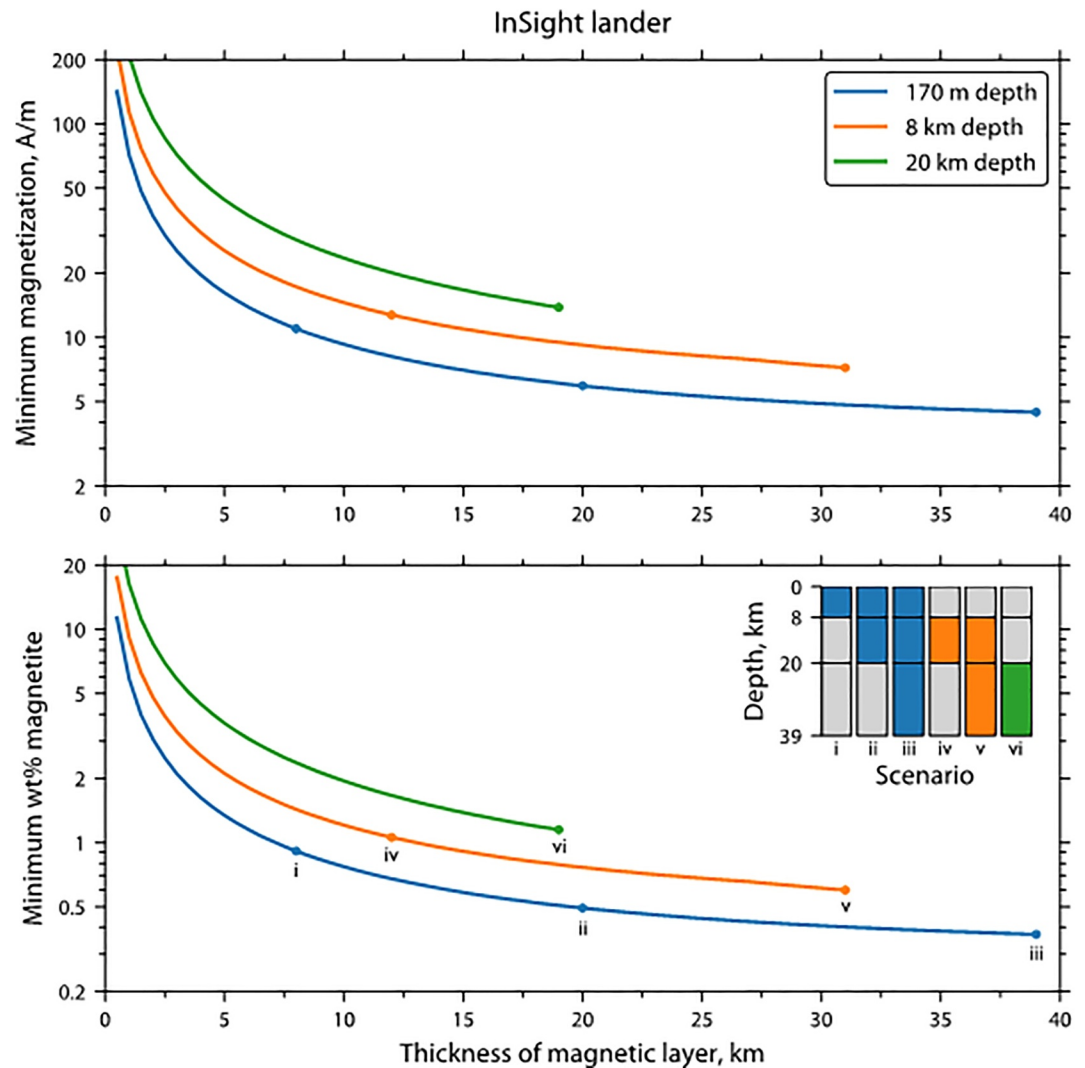


**Figure 2.** The minimum magnetization (top) and minimum abundance of magnetite (bottom) required to account for the surface field strength at the InSight landing site as a function of the thickness of the magnetized materials. The three curves correspond to the cases where the top of the magnetization is at 170 m, 8 km, and 20 km depth. The dots plotted on each curve correspond to the depths of the major seismic discontinuities for each scenario. The inset in the lower plot illustrates the distribution of magnetized materials for each of the dots plotted on the curves, with magnetized materials in color and unmagnetized materials in gray.

volume% magnetite to weight% magnetite, we assumed densities of 5,150 and 3,000 kg m<sup>-3</sup> respectively, for magnetite and the silicate minerals. For the case of the strongest orbital magnetic field above the southern highlands crust, we find that if the magnetic materials were buried 20 km below the surface and if the thickness of the magnetic layer was 40 km, 2 wt% magnetite would be needed. For a thinner magnetized layer, the required amount of magnetite could be significantly higher. For a 20 km thick layer, almost 4 wt% magnetite would be required while about 7 wt% would be required for a 10 km thick magnetic layer.

The required concentrations of magnetite to account for the magnetic field strength at the InSight lander are somewhat less. If the magnetic materials encompassed the entire 39 km thick crust, then just under 0.4 wt% magnetite would be required. In contrast, if only the deepest layer is magnetized, then about 1.1 wt% magnetite would be required.

## 4. Aqueous Alteration Results

Our aqueous alteration simulations focus on the formation of magnetite as rock dissolution progresses. Because we find that the amount of magnetite produced is strongly dependent on the assumed water-to-rock ratio, we discuss our results separately for a low ratio of 1, and for high ratios of 10, 100, and 1000. For each of these scenarios, the amount of magnetite produced is compared with the abundances required to account for the strongest magnetic field strengths measured from orbit and at the Insight landing site. We also briefly describe the other minerals that are formed. We also provide in the supplementary material figures showing the evolution of the mineralogy during the reactions (Figures S1–S13 in Supporting Information S1) and the composition of the rock at the end of the reaction in tabular form (Table S2 in Supporting Information S1) (Bultel, 2024). This allows us to compare later with what is known about the aqueous mineralogy present in the Martian crust. Note that to discuss the hydrothermal reactions and formation of magnetite, all solid solutions of iron (hydro-)oxide were investigated.

### 4.1. Low Water-To-Rock Ratios

#### 4.1.1. Dunite

Our first simulations use a water-to-rock ratio of 1 with pure water. In Figure 3a, we present the abundance of magnetite that is produced during the dissolution of ultramafic dunite protoliths with various magnesium numbers and temperatures. More details of these reactions are given in Figure S1 in Supporting Information S1 detailing the evolution of the composition of the rock during the reaction. In all cases, the weight percentage of magnetite increases with increasing dissolution, achieving a plateau value between 30% and 65% dissolution depending on temperature. After this stage of alteration, only olivine remains among the primary minerals. Magnetite production is seen to increase with decreasing Mg#. In particular, for Mg#s of 90, 79, and 75, the amount of magnetite generated after complete dissolution at 200°C was 1.7, 4.7, and 6.3 wt%, respectively. For our simulations at 100°C, we find that the amount of magnetite produced is lower by a factor of about two relative to the 200°C calculation. These abundances of magnetite are sufficient to account for the strongest magnetic anomalies observed from orbit for magnetic layer thicknesses between about 10 and 40 km (see Table 1). These abundances are also more than sufficient to account for the magnetic field strength at the InSight landing site, even for the most unfavorable case where the magnetization is located in the lowest crustal layer.

Figure 3b and Figure S1 in Supporting Information S1 show how the abundances of the other major phases evolve as the dissolution of the dunite protolith proceeds. Below 10% dissolution, minerals produced in at least trace quantities (up to ~2 wt%) are chlorite and secondary clinopyroxene. Near 10%–20% dissolution, saponite is produced as well in trace quantities. Serpentine is formed when both pyroxenes are exhausted. At ~15% dissolution, serpentine is the main mineral to form and after ~30% dissolution, both serpentine and brucite are the main minerals to form. Saponite formation starts when plagioclase is exhausted. Before this, chlorite is the main mineral that uptakes the Fe and Mg released by the dissolution of dunite. During the formation of serpentine, the chlorite is almost Mg-pure in all dunite models while it is around half daphnite-half clinocllore beforehand (Figure S2 in Supporting Information S1).

Changing the temperature of alteration and composition of the olivine does not affect the amount of serpentine produced but does somewhat impact how much brucite is formed. It also changes when and which minerals that are present in at least trace quantities start to form. The total amount of serpentine after full dissolution is about 80 wt%, whereas brucite only attains between 5 and 15 wt%. The compositions of the serpentine and brucite are shown in Figures 3c and 3d and Figure S3 in Supporting Information S1 as a function of dissolution. The wt% ratio Fe/Mg of serpentine starts high, near 90%, and depending on temperature and starting composition decreases to about 10%–30% at 60% dissolution, after which the Fe/Mg ratio remains relatively constant. In contrast, the  $\text{Fe}^{3+}/\text{Fe}_{\text{Total}}$  ratio of the serpentine starts low, near 10% (meaning 10 wt% of the Fe-serpentine is cronstedtite) and increases to about 30%–50% at 30% dissolution, after which it remains relative constant. Brucite starts to form after about 30% dissolution, with its Fe/Mg being relatively constant throughout dissolution. Depending on the starting composition and temperature, the Fe/Mg of the brucite is between 30% and 75%. Alteration at 100°C leads to higher Fe/Mg in the serpentine and brucite and to lower  $\text{Fe}^{3+}/\text{Fe}_{\text{Total}}$  in the serpentine compared to the reactions at 200°C. The lower temperature also leads to higher amounts of brucite that are formed (see Table S2 in Supporting Information S1). Lastly, we note that a higher Mg# of the starting olivine leads to a lower Fe/Mg of the serpentine and brucite, a higher amount of brucite and a higher  $\text{Fe}^{3+}/\text{Fe}_{\text{Total}}$  in the serpentine.

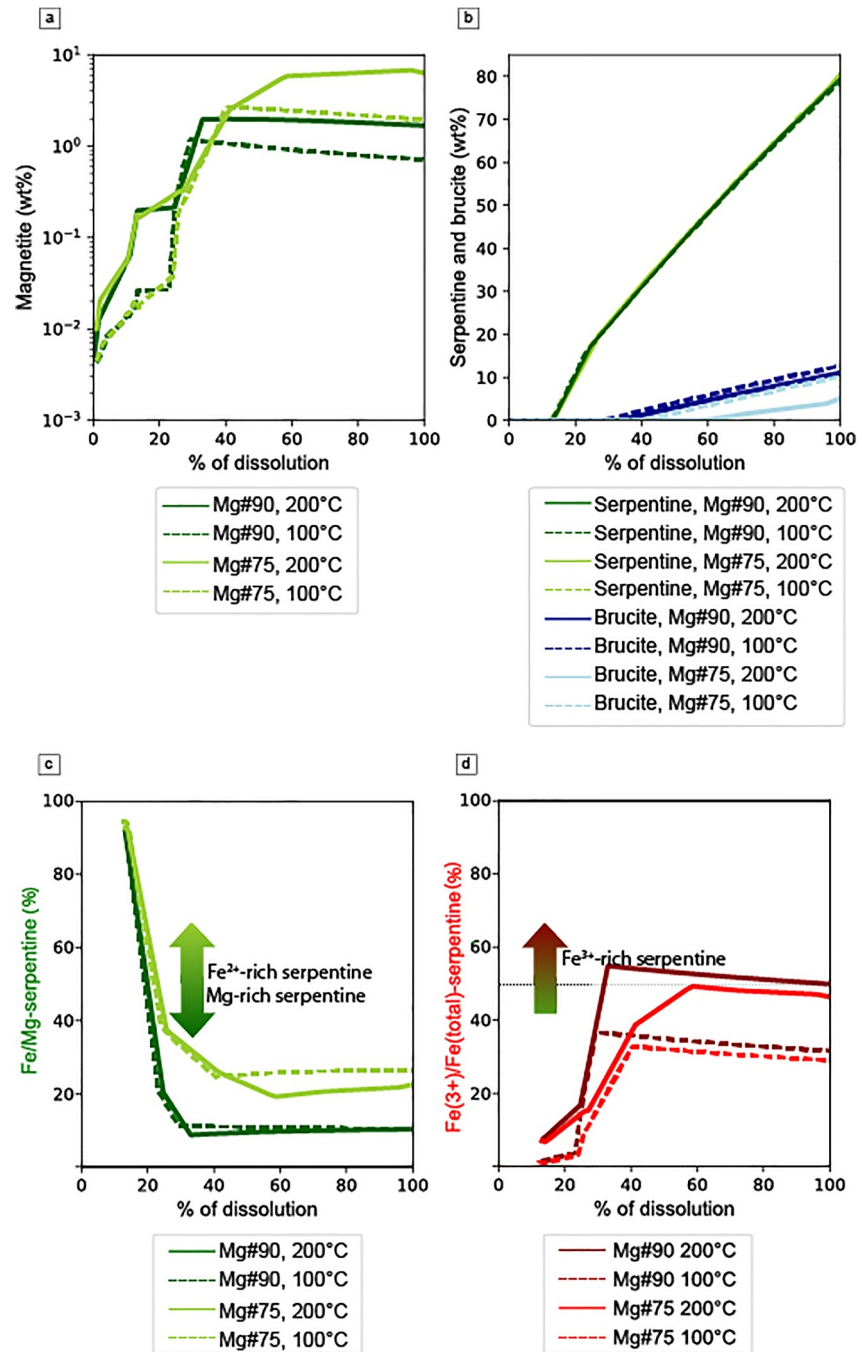


**Figure 3.** Composition and abundance of the dunite protolith alteration products as a function of dissolution. Alteration occurs at temperatures of 100 and 200°C and the Mg#s of the dunite protoliths are 75 and 90. (a) Abundances of magnetite in wt%, (b) abundances in wt% of serpentine and brucite, (c) the Fe/Mg ratio of the produced serpentine, which corresponds here to the ratio of masses of cronstedtite and greenalite to chrysotile, and (d) the Fe<sup>3+</sup>/Fe<sup>Total</sup> ratio of the serpentine which corresponds here to the ratio of masses of cronstedtite to greenalite.

#### 4.1.2. Pyroxenite and Mantle-Garnet

We next focus on the alteration of two other very mafic rocks: a pyroxenite and the mantle-garnet composition. The amount of magnetite that is produced as a function of dissolution for each of these is plotted in Figure 4a and the evolution of the rock composition is shown in Figure S4 in Supporting Information S1. For the pyroxenite, the

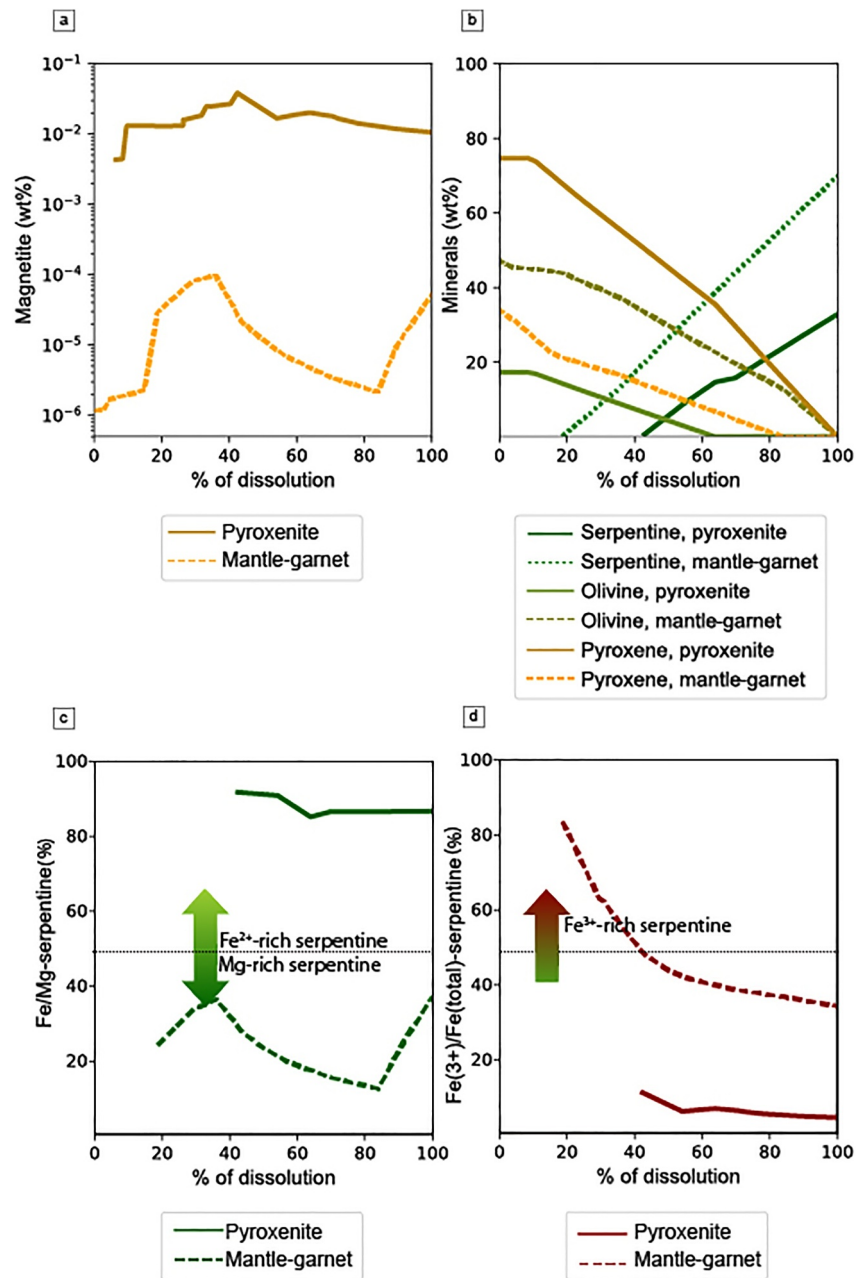


**Figure 4.** Composition and abundance of the pyroxenite and mantle-garnet protolith alteration products as a function of dissolution. (a) Abundance of magnetite in wt%, (b) abundance in wt% of serpentine, olivine, and pyroxene, (c) the Fe/Mg wt% ratio of the produced serpentine which corresponds here to the ratio of masses of cronstedtite and greenalite to chrysotile, and (d) the  $\text{Fe}^{3+}/\text{Fe}^{\text{Total}}$  ratio of the serpentine which corresponds here to the ratio of masses of cronstedtite to greenalite. Alteration occurs at a temperature of 200°C.

amount of magnetite produced is seen to be low, and remains mostly stable at around 0.01 wt%. The magnetite abundance can reach values as high as 0.04 wt% near 40% dissolution when olivine is the main mineral being altered, but even this maximal value is about two orders of magnitude lower than the amount produced when altering dunites. When considering the mantle-garnet model, the amount of magnetite produced is several orders of magnitude less than that produced by altering the pyroxenites. Thus, the amount of magnetite produced by altering pyroxenites or upper mantle compositions at 200°C and with a water-to-rock ratio of 1 is vastly insufficient to account for the magnetic anomalies observed on Mars.



The abundances of the other major phases produced by altering these two compositions are plotted in Figure 4b and Figure S4a in Supporting Information S1. In the case of the pyroxenite, chlorite and clinopyroxene are formed from the start of the dissolution. Between ~20 and ~30% dissolution, prehnite is predicted as trace, then albite (low pressure) and then talc and saponite. At 30%–40% dissolution, chlorite and secondary clinopyroxene represent up to ~10 wt% of the rock and saponite and talc are present but remain below 10 wt%. After 40% dissolution, when the pyroxene is exhausted, chlorite abundances slightly decrease and talc disappears, while secondary clinopyroxene, saponite and serpentine increase.

The abundance of serpentine increases to a maximum of 33 wt% at full dissolution. As demonstrated in Figures 4c and 4d for our 200°C simulations, the serpentine is iron-rich (i.e., Fe/Mg of ~90%) and between 5% and 10% of its iron is Fe<sup>3+</sup>. The chlorite, which is the other main mineral to uptake iron, remains at Fe/Mg around 50 before serpentine formation and is then around 45–55 when the serpentine is formed (Figure S5 in Supporting Information S1).

For the mantle-garnet composition, the main minerals to form from the start are chlorite and secondary clinopyroxene (Figure S4b in Supporting Information S1). The serpentine production starts earlier than for the pyroxenite at around 19% dissolution and attains an abundance of about 80 wt% at full dissolution. While the serpentine Fe/Mg is high at first (84%), it decreases to about 34% at full dissolution. The Fe<sup>3+</sup>/Fe<sub>Total</sub> of the serpentine varies between 13% and 37%. No brucite is formed for either of these starting compositions. The magnetite production remains low (<10<sup>-3</sup> wt%). It increases from the start until garnet is exhausted, and then it decreases until the orthopyroxene is exhausted.

In comparison to the dunite protolith, magnetite production is not favored in the pyroxenite and mantle-garnet compositions for several reasons. For the pyroxenite, the formation of serpentine is limited with a maximum of about 33 wt% being produced after full dissolution. This is compared to about 70% serpentine being produced by altering the mantle-garnet composition, and 80% when altering the dunite compositions. Furthermore, altering the pyroxenite composition produces only Fe-rich serpentine, which hinders magnetite production. While serpentine is a major product of alteration for the mantle-garnet starting composition, the serpentine is Fe<sup>3+</sup>-rich, which disfavors magnetite production. The high concentration of Fe (including Fe<sup>3+</sup>) in the serpentine produced during pyroxenite and mantle-garnet alteration leads to having a lower Fe/Si in the system to form other minerals and therefore does not promote the formation of iron (hydr-)oxides such as Fe-brucite and magnetite.

#### 4.1.3. Shergottite and Trachyte

For our last set of simulations with a low water-to-rock ratio, we consider two possible crustal rocks, one that is similar to a basaltic shergottite and the other a trachyte. As shown in Figure 5a and Figure S6 in Supporting Information S1, alteration of the shergottite protolith leads to a progressive increase in the amount of magnetite to a maximum of about 0.09 wt% near 50% dissolution. After this, the magnetite abundance decreases somewhat to about 0.05 wt% at full dissolution. The main minerals that form up to 40% dissolution are talc, albite, chlorite and secondary clinopyroxene. At 40% dissolution, the plagioclase is fully exhausted and saponite is formed at more than 1% wt. Further dissolution leads to decreasing abundances of talc and albite, while saponite, secondary clinopyroxene and chlorite increase. At ~65% dissolution and until 100% dissolution, serpentine, chlorite, saponite and secondary clinopyroxene are present at more than 10% wt. As shown in Figures 5c and 5d and Figure S6 in Supporting Information S1, serpentine and chlorite are the main Fe-rich minerals formed. Among the minerals predicted to form, serpentine is the only one to have Fe<sup>3+</sup>. The chlorite amount remains low.

When altering the trachyte protolith, the main minerals to form are sanidine, albite, secondary clinopyroxene and saponite. Talc starts to be present at more than 1% wt at ~20% dissolution and chlorite at ~30% dissolution when the plagioclase is exhausted. At 100% dissolution, sanidine and albite are present at more than 10% wt, whereas chlorite and secondary clinopyroxene are present at more than 1% wt. The quartz proportion continuously increases during dissolution to a maximum of ~10% wt. We note that only extremely trace quantities of magnetite are produced and no serpentine is produced at all.

#### 4.1.4. Summary

Our results demonstrate that magnetite is an important accessory product when altering dunitic rocks at a low water-to-rock ratio of 1. Lower Mg#s and higher temperatures of alteration give rise to the highest abundances,

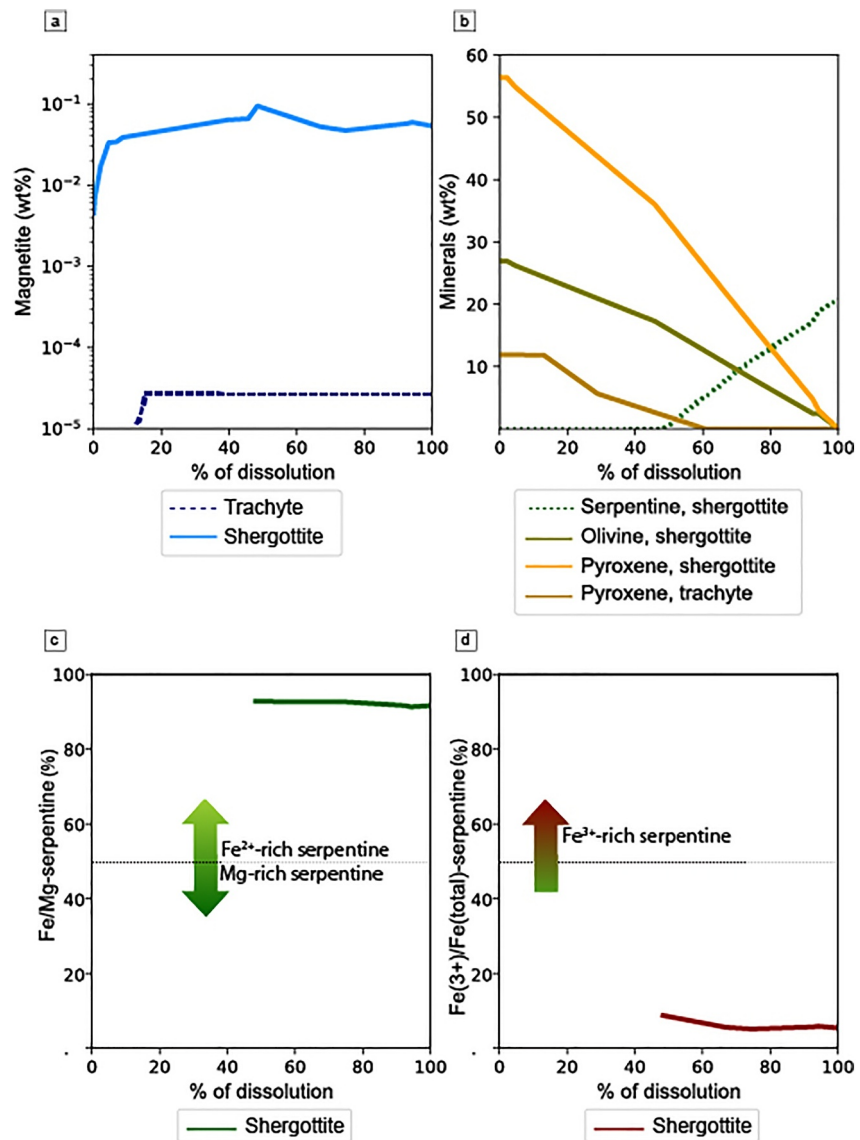


**Figure 5.** Composition and abundance of the shergottite and trachyte protolith alteration products as a function of dissolution. (a) Abundance of magnetite in wt%, (b) abundance in wt% of serpentine, olivine, and pyroxene, (c) the Fe/Mg ratio for serpentine (which corresponds here to the ratio of masses of cronstedtite and greenalite to chrysotile) when altering the shergottite protolith, and (d) the  $\text{Fe}^{3+}/\text{Fe}_{\text{Total}}$  ratio for serpentine (which corresponds here to the ratio of masses of cronstedtite to greenalite) when altering the shergottite protolith. Alteration occurs at a temperature of 200°C.

reaching up to just over 6 wt%. Such high quantities of magnetite could in principle account for the strongest magnetic anomalies observed from orbit, as well as the fields observed at the InSight landing site. However, when altering the other protoliths, magnetite is at most a trace element, even for rocks with a high amount of olivine, as in the mantle-garnet protolith (55 wt%), or with high amounts of pyroxene. After dunite, the next highest abundances of magnetite that are generated are for the alteration of a shergottite protolith. But at no more than 0.09 wt%, this could only account for surface field strengths that are weaker than those at the InSight landing site by more than a factor of 2. We note that a small amount of Fe-rich serpentine is predicted to form from the alteration of the shergottite protolith (<20 wt%). Up to about 35 wt% serpentine is also predicted to form from pyroxenite alteration and it is also Fe-rich. Finally, a large amount of serpentine is predicted when the ultramafic mantle-garnet protolith is dissolved (up to 70 wt%), but it contains a high proportion of  $\text{Fe}^{3+}$  (about a third of the iron in the serpentine). Serpentine is not predicted to form at all for alteration of the trachyte protolith.

## 4.2. High Water-To-Rock Ratios

We next consider water-to-rock ratios that are higher than 1. We start by testing the alteration of shergottite and mantle-garnet protoliths that were shown to favor the formation of serpentine at low water-to-rock ratios, but without obtaining significant amounts of magnetite. After this, we test the alteration of the pyroxenite protolith. In contrast to the previous simulations that used pure water, these simulations will make use of the simulated Martian water composition from Catling (1999) that is in equilibrium with 1 bar of CO<sub>2</sub>.

### 4.2.1. Shergottite

In Figure 6a, we show the amount of magnetite that is produced when altering a shergottite protolith at various water-to-rock ratios. While we found a maximum production of about 0.1 wt% magnetite at a low water-to-rock ratio of 1, values between 0.25 and 0.4 wt% are attained for a water-to-rock ratio of 10, with the maximum value occurring near 87% dissolution. The evolution of the rock composition during these reactions is shown in Figure S7 in Supporting Information S1. Chlorite, carbonate and quartz are the main minerals formed during alteration. At ~10% dissolution, saponite starts to form along with secondary clinopyroxene. At ~40% dissolution, when plagioclase is exhausted, the abundance of quartz strongly decreases; chlorite and carbonate slightly decrease at this point while talc and saponite start to form. At ~90% dissolution, when olivine is exhausted, serpentine (Fe-rich) is formed. At this point talc decreases, saponite increases, carbonate and chlorite values reach a plateau and magnetite slightly decreases.

For a water-to-rock ratio of 100 (see Figures S7, S8, Table S2 in Supporting Information S1), magnetite abundances of about 1 wt% are attained beyond 50% dissolution with small amounts of hematite (<0.5 wt%) being produced during the first 5% of dissolution. Chlorite, nontronite and magnetite start to form at the beginning of the dissolution. At ~50% dissolution, nontronite decreases, magnetite slightly increases and a low proportion of talc forms and then strongly increases. At ~80% dissolution, pyrite increases to reach 4% wt and only talc, chlorite and carbonate reach more than 10% wt. Both chlorite and talc are the main minerals that contain Fe.

For an even higher water-to-rock ratio of 1000, chlorite, carbonate and hematite are formed at the beginning of the dissolution. At ~40% dissolution when plagioclase is exhausted, hematite decreases while magnetite and nontronite increase. At ~90% dissolution, when olivine is exhausted, pyrite and talc increase. Magnetite production increases with dissolution, starting at about 1 wt% at 40% dissolution and reaching a maximum of around 4 wt% near 70% dissolution. For this latter simulation, we note that between 5 and 8 wt% hematite is also produced between 0% and 40% dissolution, after which it progressively decreases and disappears near 70% dissolution. Thus, aqueous alteration of the shergottite protolith could potentially account for the field strengths at the InSight lander if the water-to-rock ratio was 10 or higher. The strongest magnetic anomalies seen from orbit could also be accounted for, but only for extremely high water-to-rock ratios near 1000 and if the magnetic layer was more than 20 km thick.

Figure 6b and Figure S7 in Supporting Information S1 show how the other major phases evolve during the dissolution of the shergottite protolith for the case of a water-to-rock ratio of 10. Both pyroxene and olivine gradually decrease with increasing dissolution, disappearing entirely at full dissolution. Serpentine begins to appear only after 87% dissolution and attains a maximum of about 10 wt% at full dissolution. The serpentine is iron rich with an Fe/Mg wt% ratio of about 90% and with about 20% of its iron as Fe<sup>3+</sup> (Figures 6c and 6d). Thus, a large part of the iron from olivine and pyroxene is concentrated in the serpentine, talc and chlorite near the terminal stages of alteration (Figure S8, Table S2 in Supporting Information S1). Although the composition of the serpentine is similar to that obtained using a low water-to-rock ratio of 1, we note that significantly less serpentine is produced (10 vs. 25 wt%) and that serpentine first appears after a much higher dissolution (87 vs. 50%). We also note that serpentine is not produced at all for our simulations with water-to-rock ratios of 100 and 1000 (see Table S2 and Figure S7 in Supporting Information S1). The other main alteration minerals that contain Fe<sup>2+</sup> are chlorite, talc and carbonates (Figures S7 and S8 in Supporting Information S1).

A notable difference between the low and high water-to-rock ratio simulations is the presence of CO<sub>2</sub> in the fluid, which leads to the formation of carbonates in (at least) trace abundances. The abundance and composition of the carbonates are presented in Figure 6e as a function of the dissolution of the shergottite protolith. While carbonates are found in only trace amounts (<2 wt%) for a water-to-rock ratio of 10, they constitute a major product at the highest water-to-rock ratio of 1000, progressively increasing from 7 to 44 wt% as dissolution proceeds. For a

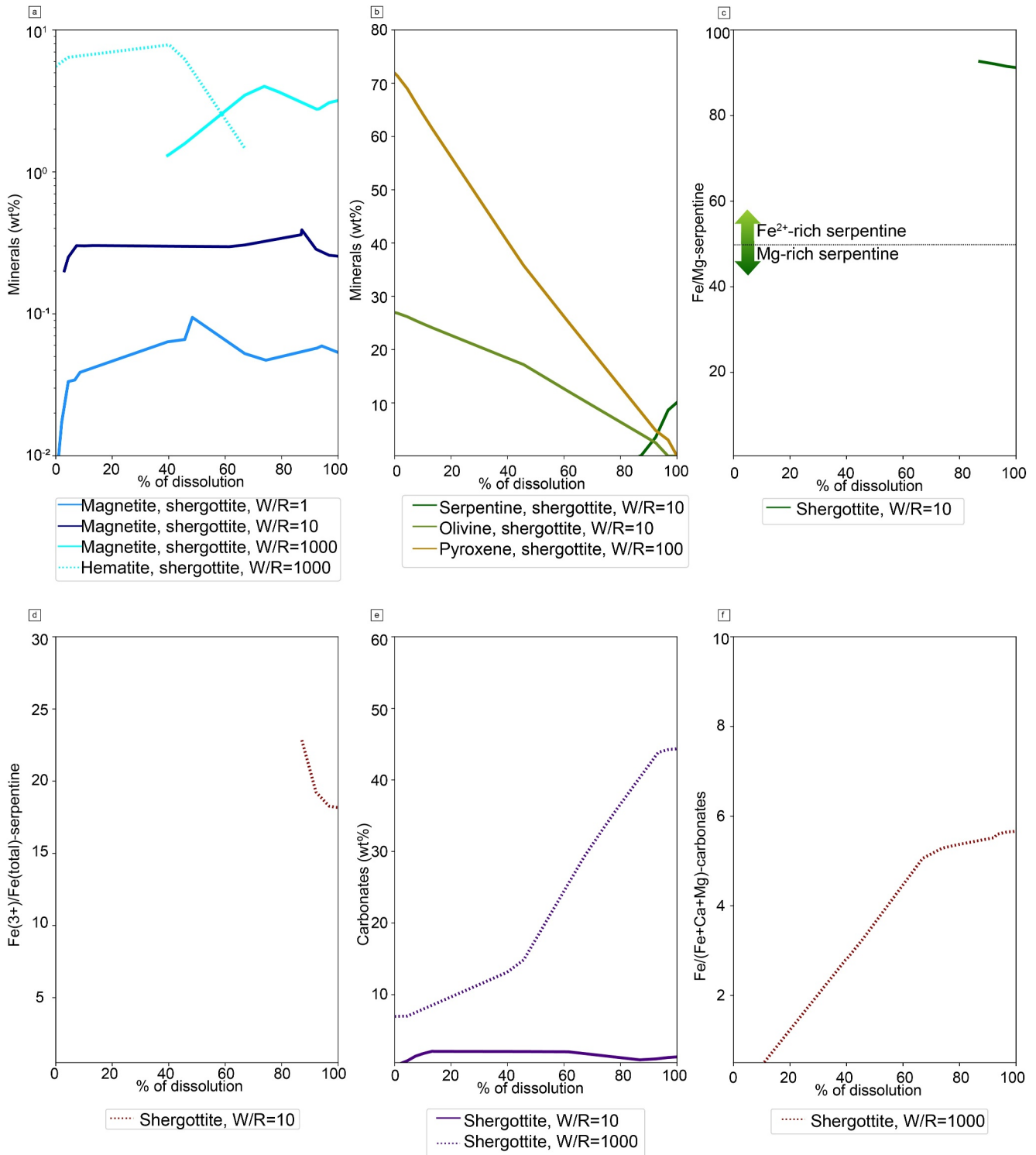


**Figure 6.** Composition and abundance of the shergottite alteration products as a function of dissolution and water-to-rock ratio. (a) Abundance in wt% of magnetite and hematite for water-to-rock ratios of 1, 10 and 1000, (b) abundance in wt% of olivine, pyroxene, and serpentine for a water-to-rock ratio of 10, (c) the Fe/Mg ratio for serpentine (which corresponds here to the ratio of masses of cronstedtite and greenalite to chrysotile) for a water-to-rock ratio of 10, (d) the Fe<sup>3+</sup>/FeTotal ratio for serpentine (which corresponds here to the ratio of masses of cronstedtite to greenalite) for a water-to-rock ratio of 10, (e) abundance of carbonates in wt% for water-to-rock ratios of 10 and 1000, and (f) the Fe/(Fe + Ca + Mg) ratio of the carbonates (which corresponds here to the ratio of masses of siderite to siderite, calcite and magnesite) for water-to-rock ratios of 10 and 1000. The Fe/(Fe + Ca + Mg) ratio of the carbonates is not shown for a water-to-rock ratio of 10 because they are present only in trace quantities. Alteration occurs at a temperature of 200°C.

water-to-rock ratio of 10, the Fe/(Fe + Mg + Ca) wt% ratio of the carbonates is close to 20% when the rock dissolution is less than 20% and is close to 5% for higher dissolutions. In contrast, for a water-to-rock ratio of 1000, Fe/(Fe + Mg + Ca) progressively increases from about 0% to 6% at full dissolution (Figure 6f). As the water-to-rock ratio increases, the abundance of carbonates formed also increases. This is due to the fact that the alteration reactions are progressively controlled by the composition of the solution.

#### 4.2.2. Mantle-Garnet

We next assess the alteration of the ultramafic mantle-garnet protolith at various water-to-rock ratios (Figure 7, Figure S9 and Table S2 in Supporting Information S1). For a low water-to-rock ratio of 1, magnetite is only produced in extreme trace quantities, and higher water-to-rock ratios of 10–1000 produce even lower amounts (Figure 7a). For the lowest water-to-rock ratio, the maximum amount of magnetite produced is about  $10^{-4}$  wt%, and for the higher water-to-rock ratio, the magnetite abundance is lower by several orders of magnitude. Similar to the case of the shergottite protolith, we note that hematite is predicted to be a major phase for the highest water-to-rock ratio of 1000, being close to 10 wt% at all stages of dissolution. For a water-to-rock ratio of 100 (not plotted), magnetite abundances of only about  $10^{-7}$  wt% are reached, with small amounts of hematite (around 1 wt%) being produced during the first 10% of dissolution.

The abundance of serpentine is shown in Figure 7b and Figure S9 in Supporting Information S1 as a function of dissolution of the mantle-garnet protolith for a water-to-rock ratio of 10. The abundance of olivine and pyroxene is seen to progressively decrease, disappearing entirely at full and 80% dissolution, respectively. Chlorite and carbonate are formed from the start of dissolution, and quartz and nontronite are only predicted between ~15% and ~18% dissolution. At ~20% dissolution, talc, amphibole, serpentine and secondary clinopyroxene first appear. Talc is then dissolved at ~30% dissolution when olivine is fully exhausted. Serpentine reached a maximum of 80 wt% at full dissolution. Before 25% dissolution, the serpentine is Fe-rich with a Fe/Mg wt% ratio close to 90% and with up to 46% of its iron as  $\text{Fe}^{3+}$  (Figures 7c and 7d). The serpentine Fe/Mg then decreases with increasing dissolution, with about 50% at 40% dissolution and ending at about 40% at full dissolution with about 25% of the iron as  $\text{Fe}^{3+}$ . Magnetite formation is favored during the dissolution of olivine and during an important increase in talc and serpentine. After that, the magnetite proportion slightly decreases and then stabilizes. Note that the amount of magnetite remains very low.

At a water-to-rock ratio of 100, chlorite and carbonate are predicted to form from the start as major phases. Nontronite is predicted to dissolve between 5% and 30%, after which, talc is predicted to increase when olivine is exhausted. Hematite is also formed from 0% to 10% dissolution as well as between 30% and 45% dissolution. Pyrite forms between 45% and 55% dissolution. We note that serpentine starts from at 55% dissolution and reaches up to 44 wt% at 100% dissolution. At a water-to-rock ratio of 1000, carbonate, hematite and chlorite are the main minerals formed. At ~30% dissolution, olivine is exhausted and magnetite increases. From 40% to 70% dissolution, nontronite is predicted and from 50% to full dissolution, talc is predicted to form.

Talc, chlorite, carbonate, nontronite and serpentine are the main minerals that have  $\text{Fe}^{2+}$  in these simulations. No serpentine is predicted to form for a water-to-rock ratio of 1000 (Table S2 and Figures S9, S10 in Supporting Information S1).

The abundance and composition of the carbonates produced when altering the mantle-garnet type rocks are shown in Figures 7e and 7f. Although only trace amounts (<2 wt%) are produced for a water-to-rock ratio of 10, they constitute up to 48 wt% of the rock at full dissolution for a water-to-rock ratio of 1000. For a water-to-rock ratio of 10, Fe/(Fe + Mg + Ca) of the carbonates is always close to 20%, but for a water-to-rock ratio of 1000, this progressively increases to about 50% at full dissolution.

#### 4.2.3. Pyroxenite

Next, we investigate the alteration of a pyroxenite protolith at high water-to-rock ratios (Figure S11 in Supporting Information S1). At a low water-to-rock ratio of 1, we previously found that a maximum of 0.04 wt% magnetite was produced. In Figure 7a, it is seen that increasing the water-to-rock ratio leads to progressively higher amounts of magnetite. A water-to-rock ratio of 10 increases the abundance of magnetite by almost an order of magnitude, attaining a maximum of 0.26 wt% at around 30% dissolution, after which it decreases to 0.06 wt% at full dissolution.



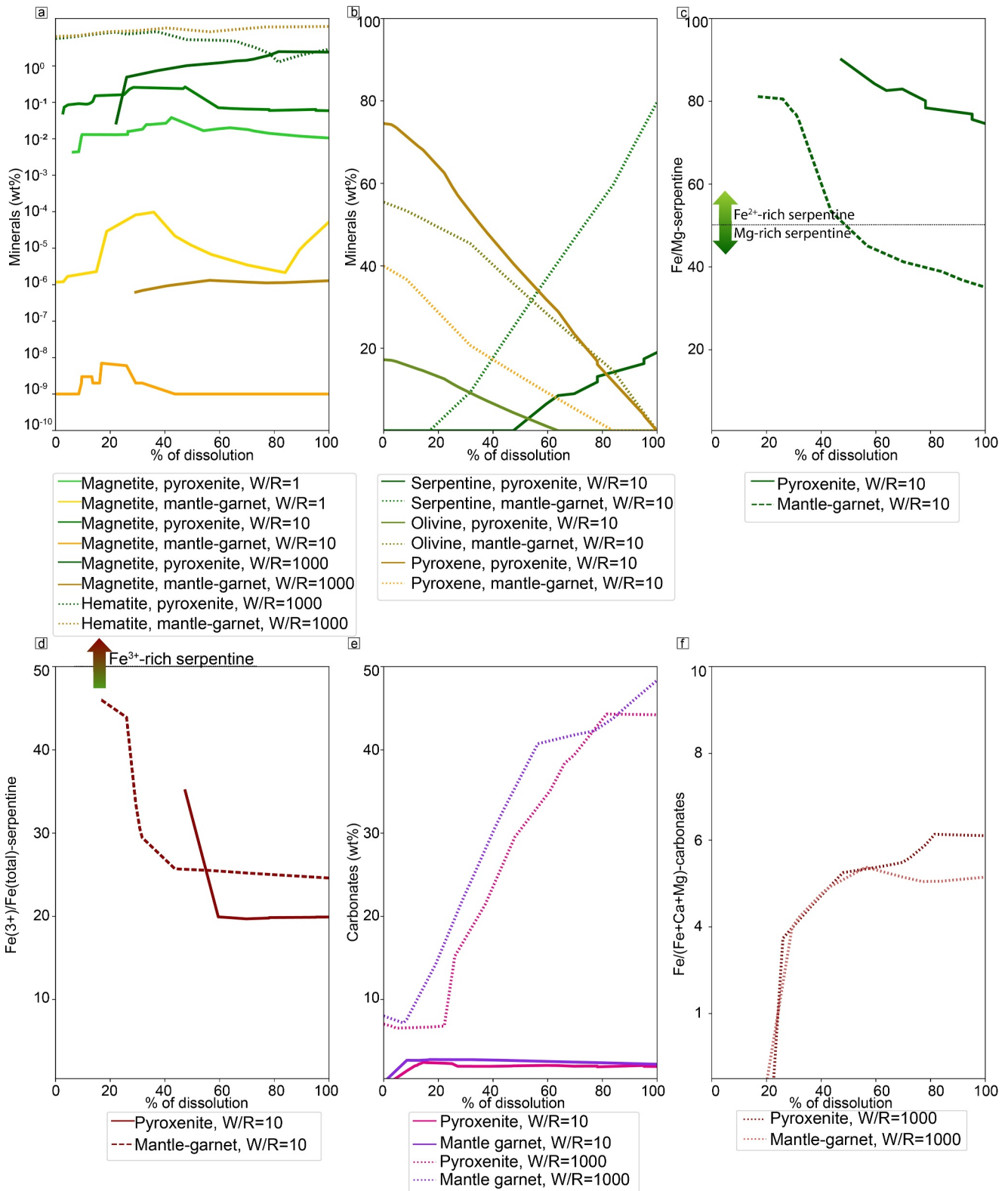


Figure 7.

Carbonate and chlorite form at the beginning of the reaction up to 100% dissolution. A few other minerals are predicted to form from the start as well, but then their abundance decreases and they completely dissolve. Among them are quartz (up to 40% dissolution), beidellite (up to 10% dissolution), and nontronite (up to 25% dissolution). Sanidine is predicted between 10% and 35% dissolution. Albite low forms between 20% and 25% dissolution and prehnite between 15% and 25% dissolution. Secondary clinopyroxene forms from 20% dissolution and then increases up to 25wt% at 65% dissolution. Saponite forms from 25% dissolution and reaches 10 wt% at 65% dissolution.

The abundances of serpentine, olivine and pyroxene are shown in Figure 7b as a function of dissolution of the pyroxenite protolith for a water-to-rock ratio of 10. The abundance of olivine and pyroxene is seen to progressively decrease, disappearing entirely at around 60% and full dissolution, respectively. Serpentine first appears near 50% dissolution and increases to a maximum of 20 wt% at total dissolution. The serpentine is Fe-rich with a Fe/Mg wt% ratio close to 90% and with up to 35% of its iron as Fe<sup>3+</sup> (Figures 7c and 7d). The Fe/Mg of the serpentine decreases to about 75% at total dissolution with about 20% of the iron as Fe<sup>3+</sup>. From 60% to 100% dissolution, the assemblage is mainly constituted of serpentine, secondary clinopyroxene, chlorite, carbonate and saponite with traces of magnetite and chromite.

For a water-to-rock ratio of 100, carbonate and chlorite are predicted to form from the start of the reaction and increase during the first 20% dissolution to a plateau value around 15–20 wt%. Hematite is also predicted in trace quantities (<1wt%) at the beginning of the reaction but disappears at 5% dissolution. Diaspore is predicted as trace (<1wt%) only between 5% and 10% dissolution. At 5% dissolution, nontronite is formed and reaches a few wt% and then decreases at 80% dissolution and is absent after 90% dissolution. Magnetite appears at 5% dissolution. It reaches 1 wt% near 85% dissolution with a maximum of around 2 wt% at 100% of dissolution (not plotted, see Figure S2, S7, and Table S2 in Supporting Information S1). It decreases slightly between 10% and 20% dissolution when beidellite is formed as trace (<1wt%) but then increases to a plateau value until 70% dissolution when it increases again continuously until the end of the reaction. Quartz is formed from 15% dissolution and reaches around 4 wt% and then decreases from 40% dissolution and is absent after 70% dissolution. Talc forms at 30% dissolution and increases until becoming the major secondary mineral present after 40% dissolution. It reaches up to 67wt% at the end of the reaction.

A water to rock ratio of 1000 gives rise to a maximum of 2.5 wt% magnetite near 80% of dissolution. Like our previous simulation with a water-to-rock ratio of 1000, we note that hematite is also predicted to be a major phase, especially below 50% of dissolution, with abundances between 5 and 8 wt%. The abundance of hematite decreases as dissolution progresses, disappearing near 70% dissolution. Chlorite, carbonate and hematite form at the beginning of the reaction. Nontronite appears at ~40% dissolution when the hematite is decreasing. Pyrite forms at ~70% dissolution but remains minor. Talc is predicted to form at ~80% dissolution. For a water-to-rock ratio of 10, serpentine, chlorite and talc are the main minerals that integrate iron (Figure 7 and Figure S12 in Supporting Information S1). For both water-to-rock ratios of 100 and 1000, talc is the main secondary mineral containing iron, while chlorite and carbonate that also contain iron are predominantly Mg and Ca rich respectively (Figure 7 and Figure S12 in Supporting Information S1). No serpentine is predicted to form for water-to-rock ratios of 100 and 1000.

The abundance and composition of the carbonates produced when altering the pyroxenite composition are shown in Figures 7e and 7f. Although only trace amounts (around 2 wt%) are produced for a water-to-rock ratio of 10, they constitute up to 18% for a water-to-rock ratio of 100 and up to almost half of the rock at full dissolution for a water-to-rock ratio of 1000. Throughout the dissolution process, the predominant carbonate present is magnesite, comprising 64%–75% of the total carbonate content, while siderite makes up less than 6%.

**Figure 7.** Composition and abundance of the pyroxenite and mantle-garnet alteration products as a function of dissolution and water-to-rock ratio. (a) Abundance of magnetite and hematite in wt% for water-to-rock ratios of 1, 10, and 1000, (b) abundance of olivine, pyroxene, and serpentine in wt% for a water-to-rock ratio of 10, (c) the Fe/Mg ratio for serpentine (which corresponds here to the ratio of masses of cronstedtite and greenalite to chrysotile) for a water-to-rock ratio of 10, (d) the Fe<sup>3+</sup>/Fe<sub>Total</sub> ratio for serpentine (which corresponds here to the ratio of masses of cronstedtite to greenalite) for a water-to-rock ratio of 10, (e) abundance of carbonates in wt% for water-to-rock ratios of 10 and 1000, (f) the Fe/(Fe + Ca + Mg) ratio of the carbonates (which corresponds here to the ratio of masses of siderite to siderite, calcite and magnesite) for water-to-rock ratios of 10 and 1000. Note that the Fe/(Fe + Ca + Mg) ratio of the carbonates is not shown for a water-to-rock ratio of 10 because they are present in only trace quantities. Alteration occurs at a temperature of 200°C.

#### 4.2.4. Trachyte and Dunite

We considered the alteration of the trachyte protolith at higher water-to-rock ratios, but these conditions did not lead to a significantly increased production of magnetite compared with the low water-to-rock simulations. Because the total abundance was extremely low ( $<10^{-12}$  wt%), we do not plot the results or discuss these simulations. Furthermore, we do not present the alteration of dunitic protoliths with higher water-to-rock ratios. Although these simulations produce more magnetite than the low water-to-rock simulations, magnetite production at low water-to-rock ratios is already sufficient to account for the strongest Martian magnetic anomalies. It is also probably unlikely that dunites would be found in an environment with a high water-to-rock ratio. Such rocks would likely form at a great depth in the crust, away from any large standing body of water, and would also form with a low porosity and thus have a low water-holding capacity. Nevertheless, we note that locally on Mars surface rocks with high amounts of olivine, such as olivine cumulates, have been documented at the surface of the planet. These rocks, however, are not representative of the crust where strong magnetic anomalies are seen (Liu et al., 2022).

#### 4.2.5. Summary

The amount of magnetite that is produced during aqueous alteration generally increases as the water-to-rock ratio increases (Table S2 and Figure S13 in Supporting Information S1). For shergottite protoliths, and for respective water-to-rock ratios of 1, 10, 100 and 1000, it is possible to produce up to 0.1, 0.4, 1, and 4 wt% magnetite. Similar results were obtained for pyroxenite protoliths, where using the same water-to-rock ratios, up to 0.04, 0.26, 2, and 2.5 wt% magnetite were produced. In contrast, only trace quantities of magnetite were produced for the mantle-garnet and trachyte protoliths at high water-to-rock ratios. Shergottites and pyroxenites could thus potentially account for the measured magnetic field strength at the InSight lander if alteration occurred with a water-to-rock ratio of 10 or more. These protoliths could potentially account for the strongest orbital magnetic field strengths if alteration occurred with an extremely high water-to-rock ratio of 100, but only if the magnetic layer was more than about 40 km thick. The amount of serpentine that is generated at water-to-rock ratios of 1 and 10 are broadly similar. However, given that the initial fluid was assumed to be in equilibrium with the Martian atmosphere, significant quantities of carbonates can be produced at high water-to-rock ratios. Although carbonates make up only a few wt% at a water-to-rock ratio of 10, they can make up almost half of the rock at a water-to-rock ratio of 1000.

## 5. Discussion

### 5.1. Magnetization of Martian Rocks and Meteorites

The Martian meteorites are, with few exceptions, Amazonian in age ( $<3$  Ga) and hence likely formed when the core dynamo field of Mars was no longer active (see McSween and McLennan (2014) and Udry et al. (2020) for reviews of these meteorites). While these rocks are unlikely to sample the magnetized materials that are responsible for the observed magnetic anomalies, one can test if these lithologies could account for the observed field strengths if they formed earlier when a dynamo field was present. The large number of meteorites with such measurements (about 50) ensures that these rocks sample many different locales on Mars.

To address this, we make use of the approach employed by Rochette et al. (2005) and Gattacceca et al. (2014) that relies on the measured saturation remanent magnetization of the rock. In particular, we make use of an empirical relation between acquired remanent magnetization, the ambient field strength, and the rock saturation remanent magnetization.

$$\frac{M_r}{M_{rs}} = \frac{B}{a}, \quad (2)$$

where the constant  $a$  is the same as in Equation 1. The saturation remanent magnetization,  $M_{rs}$ , is the maximum remanent magnetization that the rock can acquire and is easily measured in the laboratory. It depends upon both the saturation remanent magnetizations of the magnetic minerals in the rock and their abundances. Using Equation 1, we first estimated the minimum saturation remanent magnetizations that are required to account for the strongest orbital magnetic field and the observed field at the InSight landing site, assuming a magnetizing field strength of 50  $\mu$ T. These values are tabulated in Table 1 for the same scenarios that were previously investigated.

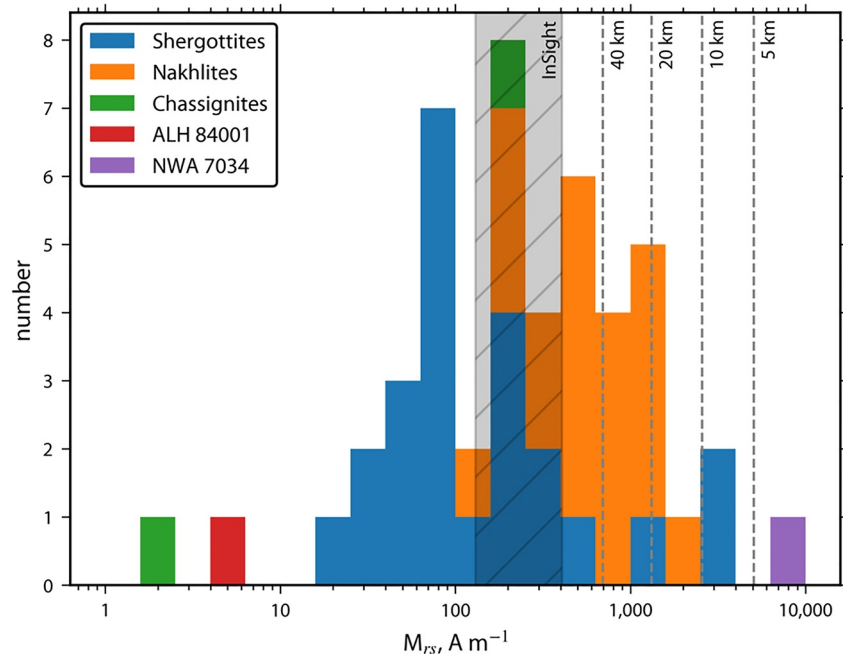


**Figure 8.** Histogram of Martian meteorite saturation remanent magnetizations,  $M_{rs}$ , whose values are taken from Table S4 in Supporting Information S1. The cross-hatched region represents the minimum values that would be required to account for the observed magnetic field at the InSight landing site if one or more of the three crustal layers there obtained a chemical remanent magnetization in a  $50 \mu\text{T}$  field. The four dashed vertical lines correspond to the minimum thicknesses of magnetized crust to account for the strongest orbital magnetic anomaly for the same conditions of magnetization acquisition. Colors differentiate the different meteorite classes.

We next compared these values with those obtained from analyses of Martian meteorites. These were taken from the measurements tabulated in Rochette et al. (2005), Gattacceca et al. (2014), Herd et al. (2017), and Krämer Ruggiu et al. (2020), and we included 13 new measurements. The complete database is described in Appendix A and Table S4 in Supporting Information S1. In total, there are  $M_{rs}$  measurements for 48 distinct meteorites, and these were converted from units of  $\text{A m}^2 \text{kg}^{-1}$  to  $\text{A m}^{-1}$  by using an appropriate rock density. The meteorite saturation remanent magnetizations, as well as the required values to account for the orbital and surface magnetic field measurements, are summarized in Figure 8.

We first consider the strongest magnetic field strengths observed from orbit over the southern highlands of Mars. If the magnetic layer there was 40 km thick, which is implausibly high for the case of hydrothermal alteration, we find that just over one-fifth (11 of 48) of the meteorites could potentially account for the required minimum magnetizations. If the thickness of the magnetic layer was 20 km, then 5 of the 48 meteorites could account for the observed magnetizations (2 shergottites, 2 nakhrites, and NWA 7034). For a magnetic layer thickness of 10 km, the number of meteorites reduces to 3: Two of these are shergottites that do not show evidence for hydrothermal alteration, and the third is the NWA 7034 highland breccia. NWA 7034 is sufficiently magnetic that only a 5 km layer composed of this material is necessary to account for the strongest orbital magnetic anomaly.

NWA 7034 is unique among the Martian meteorites in that it contains zircons and igneous lithologies that date from 4.39 to 4.47 Ga and that its bulk composition is similar to the bulk crustal composition of Mars (e.g., Agee et al., 2013; Bellucci et al., 2015; Bouvier et al., 2018; Humayun et al., 2013; McCubbin et al., 2016; Nyquist et al., 2016). It contains a combined amount of about 15 wt% magnetite and maghemite, of which the latter was formed by low-temperature aqueous alteration (Agee et al., 2013; Gattacceca et al., 2014). This meteorite contains about an order of magnitude more water than the other Martian meteorites (Agee et al., 2013) and materials of this composition are plausibly responsible for the strong remanent magnetic fields observed in the southern highlands of Mars (Gattacceca et al., 2014).

In contrast to the strongest magnetic fields that are found over the southern highland crust, there are many more Martian meteorites that could account for the weaker field strength measured at the InSight landing site in the

northern lowlands of Mars. If the magnetic layer there comprised the entire 39 km thick crust, then about two-thirds of the Martian meteorites (32 of 48) would have the required minimum saturation remanent magnetizations to account for the observed surface field strength if they formed in the presence of a 50  $\mu\text{T}$  ambient field. Of these, about one-third are shergottites, with most of the remainder being nakhlites. It must be noted that nakhlites are strongly overrepresented compared to shergottites in the database used for Figure 8, with a nakhlite/shergottite ratio of 0.83 (20/24) compared to 0.11 (32/300) in the entire Martian meteorite collection. If only the lowermost layer of the crust (from 20 to 39 km depth) were magnetized, then just under half of the Martian meteorites (19 of 48) could potentially account for the observed field strength. Thus, lithologies comparable to the known Martian meteorites could likely account for the observed magnetic field strength at the InSight landing site, and by analogy, elsewhere in the northern lowlands.

Lastly, we note that the abundance of magnetite has been measured in situ for some rocks in Gale crater by the Curiosity rover and in Gusev crater by the Spirit rover. As summarized in Rampe et al. (2020), some of the sandstone deposits in Gale crater contain up to 11 wt% magnetite. This magnetite is interpreted to be the result of complex near-surface aqueous alteration processes that involved the dissolution of olivine. Even though the abundance of magnetite in these sedimentary rocks is high, with deposit thicknesses on the order of 100 m, they would not be able to account for the strongest magnetic anomalies measured from orbit. They would also make only a small contribution to the surface field strength in comparison to the field strengths measured at the InSight landing site. High abundances of magnetite have also been reported for some basalts within the Gusev crater. The average abundance of magnetite for 16 rocks is about 3 wt%, with the highest values being close to 9 wt% (McSween et al., 2008). Based on their Ti content, this magnetite is interpreted to be a primary magmatic mineral (Morris et al., 2008). Taking into account the reduced saturation remanent magnetization of titanomagnetite with respect to pure magnetite, basalts with these compositions could potentially account for the strongest magnetic anomalies measured from orbit if the deposits were 10s of km thick.

## 5.2. Can Magnetite Production by Hydrothermal Processes Explain the Martian Magnetic Anomalies?

Hydrous alteration of known rock types that are found on Mars can, in certain circumstances, lead to the generation of high quantities of magnetite. For almost all the scenarios that we considered, magnetite is the only magnetic mineral that is produced. Minerals such as pyrrhotite or maghemite are never observed, and hematite is only observed in the most extreme cases when the water-to-rock ratio is near 1000. When the protolith is dunitic, sufficient magnetite can be generated to account for the strongest observed magnetic anomalies when using low water-to-rock ratios. In contrast, alteration of compositions similar to the basaltic shergottites and pyroxenites with higher water-to-rock ratios can account for the field strengths observed at the InSight landing site.

When considering a low water-to-rock ratio of 1%, 30%–40% dissolution of a dunitic protolith can generate about 2 wt% magnetite for a variety of protolith Mg#s and alteration temperatures. With this abundance, the strongest magnetic anomalies on Mars could be accounted for by a magnetic layer that is about 40 km thick. Our simulations show that magnetite production is favored when the alteration occurs at high temperatures and for decreasing Mg# of the olivine. This phenomenon is supported by the observation of terrestrial samples (Klein et al., 2014), laboratory experiments (i.e., McCollom et al., 2020) and geochemical models (i.e., McCollom et al., 2022). By changing the Mg# of the olivine from 90 to 75, we find that the amount of magnetite that is produced can be increased by about a factor of two. In particular, just over 6 wt% magnetite can be generated after about 50% dissolution of a dunitic protolith at 200°C for the lowest Mg# that we considered. This abundance is comparable to the amount of magnetite in the most magnetic Martian meteorite NWA 7034. Furthermore, at 6 wt% magnetite, the strongest magnetic anomalies could be accounted for by a layer of this material that was about 10 km thick.

For a water-to-rock ratio of 1, none of the other protoliths that we investigated could generate enough magnetite to account for the strongest magnetic anomalies detected from orbit or at the InSight landing site. When increasing the water-to-rock ratio to 10, none of the other protoliths generated enough magnetite to account for the strongest magnetic anomalies either, but some could account for the weaker anomaly at the InSight landing site. In particular, hydrous alteration of our pyroxenite protoliths generated up to 0.3 wt% magnetite, and alteration of the shergottite protoliths generated up to 0.4 wt% magnetite. With these abundances, the magnetic field strength observed at the InSight landing site could be accounted for if the entire 39 km thick crust was magnetized.



By increasing the water to rock ratio to 100, alteration of the shergottite and pyroxenite protoliths generated even more magnetite, between about 1 and 2 wt%. At an even higher water-to-rock ratio of 1000, alteration of the shergottite protolith generated up to 4 wt% magnetite. Though 4 wt% could in principle account for the strongest magnetic anomalies detected from orbit if the magnetic layer was more than 20 km thick, such water-to-rock ratios are probably unrealistically high for geologic units that are 10–100s of kilometers in size in the southern highlands. Aqueous alteration of the upper mantle protolith never generated enough magnetite to account for either the strong fields measured from orbit or at the InSight landing site. This suggests that mantle materials excavated by large impact basins are unlikely to be responsible for any of the Martian magnetic anomalies. Similarly, aqueous alteration of the felsic trachyte protolith only generated trace amounts of magnetite and is unlikely to be responsible for any of the Martian magnetic anomalies.

### 5.3. Previous Predictions of Magnetite Production by Alteration of the Martian Crust

While numerous studies already model hydrothermal reactions of the Martian crust, none of them focus primarily on the production of magnetite. All these studies already noted the general trend reproduced in our study, which is the increase in the production of magnetite with increasing water-to-rock ratio, temperature and amounts of mafic minerals in the starting composition. Griffith and Shock (1995, 1997) studied several starting rock compositions for Mars with temperatures (150°–250°C) close to the work presented here. As in our models, magnetite is predicted to form in small amounts when a rock with a Shergottite composition is altered at 200–250°C. More magnetite is predicted to form for higher water-to-rock ratios. More notable amounts of magnetite (10s mol %) are predicted to form when altering a rock with a Chassigny (dunitic) composition, with the abundance increasing with increasing water-to-rock ratio. These trends of higher amounts of magnetite with a higher water to rock ratio and for more (ultra)mafic compositions fit well with the models presented here. Our models include starting compositions more representative of the diversity of the Martian crust and do not consider whole rock chemistry but instead mineralogical compositions and therefore the thermodynamic constant of minerals. It also considers a more complete database for possible secondary products (e.g., solid solution of serpentine and carbonate). These improvements seem to lower the amount of magnetite predicted for both shergottite (around 10 mol% in Griffith & Shock, 1997 and around 2 mol% here for W/R of 1000) and dunitic (10s mol% in Griffith & Shock, 1997 and around 1 mol% here for W/R of 1000 of pyroxenite) compositions and to increase the amount of Fe-bearing clay minerals.

The study by Schwenzer and Kring (2009) that focused on impact generated hydrothermal systems also reported trends that fit our models. The iron oxide predicted to form increases with the water-to-rock ratio and even dominates for a water-to-rock ratio >10,000. They also note an increasing amount of hematite at high water-to-rock ratios, while magnetite is rather formed at water-to-rock ratios between about 30 and 100. Hematite production is also predicted in Bridges and Schwenzer (2012) for high water-to-rock ratios (>10) when altering a rock with a Nakhla composition (which is close to the pyroxenite used in our model). We confirm this here and additionally show that magnetite is favored over hematite for lower water-to-rock ratio for most of the composition seen for the martian crust.

Focusing on the alteration mineralogy seen at Gale Crater, Bristow et al. (2015) predicted high amounts of magnetite (up to 6.8 wt% at 130°C and W/R of 100) and Fe-rich clay minerals for water-to-rock ratios from 10 to 100 at temperatures between 50 and 130°C). Magnetite production was found to increase with increasing temperatures and water-to-rock ratios (from traces to 5.2 wt%) as it does in most of our models. This trend is also reported in Zolotov (2007, 2012) who shows for a CI composition an increase of magnetite production with an increase of temperature of alteration at a water-to-rock ratio of 1. Our results suggest that this is also valid for a wide range of starting compositions. However, we also show that magnetite is not predicted as more than a trace for trachyte or mantle-garnet compositions as starting materials.

### 5.4. Comparison With Aqueous Alteration Products Observed on Mars

Throughout most of this study, we have focused on the amount of magnetite that could be generated by altering various rock types. Here, we focus instead on the other minerals that are produced and then compare these with the mineral assemblages of altered rocks that have been detected on the surface of Mars. For simplicity, we review the mineralogy of the alteration products when the protolith is fully dissolved. Though the relative proportions of the alteration products would be slightly different at partial dissolution, this would not affect the overall results

discussed here. Furthermore, we neglect phases with abundances that are less than one weight %, as these would be difficult to detect by most remote sensing techniques. It is important to keep in mind that when discussing detection by remote sensing, our view of the surface of Mars is biased notably by the uneven coverage of surface images and that the surface is often hidden by dust (Carter et al., 2013).

The case of altering the trachyte protolith found at Gale Crater stands out compared to our other results for a low water-to-rock ratio. It is the only case where the main products of alteration are not hydrated but are instead low-temperature phases of feldspar (albite-low and sanidine), with the other products in decreasing order being quartz, secondary clinopyroxene, and chlorite. Chlorite is the main hydrated mineral, but it represents less than 6 wt% of the final mineralogical assemblage. Hydrothermal alteration of a trachyte will therefore generate only low abundances of hydrated material (di-tri-Fe, Mg-phyllsilicates) and this coincides well with the mineralogy of the alteration products that have been documented so far at Gale Crater (Bristow et al., 2018). The only exception is the detection of several sulfates, akaganeite and carbonates that were reported in the crater (McAdam et al., 2020), suggesting that S, Cl, and C, which were not included in our model, would be necessary to better represent the entire mineralogical assemblage seen at Gale Crater. Regardless, we note that the minerals missing in our models are all suggested to come from later diagenesis processes possibly involving warm saline fluid in a lacustrine environment (e.g., McAdam et al., 2020) and are unlikely to be hydrothermal alteration products. Sulphide alteration has led to limited sulfate formation or mobilized S, Cl and other mobile elements (Berger et al., 2017; Yen et al., 2021) and formation of hydrothermal feldspar, silica and some clays have been documented at Gale Crater (Morris et al., 2016, 2020; Rampe et al., 2020). However, these observations are sparse and are not accompanied by detection of prehnite, chlorite, serpentine, or other typical hydrothermal minerals.

The case of dunite alteration at low water-to-rock ratios is also particular in that these are the only protoliths that produce hydroxide brucite (up to about 10 wt%). Serpentine, chlorite, secondary pyroxene and oxides are also predicted to form (in decreasing order of abundances), with serpentine representing more than 79 wt% of the resulting rock. Known serpentine detections on Mars are usually found in association with large quantities of the clays saponite, chlorite, nontronite, and talc, along with possible carbonates (Amador et al., 2018; Bishop et al., 2013; Bultel et al., 2015; Ehlmann et al., 2010; Michalski & Niles, 2010). This suggests that dunite is probably not the main starting protolith where serpentine is found on the surface. If hydrous alteration of dunites is responsible for the generation of large quantities of magnetite, then these materials would need to be buried at some depth in the crust in order to avoid detection by remote sensing techniques. Note that most studies reporting observations of serpentine on Mars rely on impact craters in order to have access to deep crustal material, yet no observations match the assemblages seen here for dunites.

Similar to dunites, the alteration of the mantle-garnet protolith at low to moderate water-to-rock ratios also produces serpentine as the dominant major product (about 70–80 wt%), which is associated with secondary clinopyroxene, amphibole, carbonate, and chlorite. The low abundances of other phyllosilicates besides serpentine and the presence of amphibole are unusual for Martian serpentine detection at the surface. At the highest water-to-rock ratios, alteration of the mantle-garnet protolith generates mainly carbonates, talc, hematite and chlorite. This corresponds well to the carbonated serpentine reported locally in the Nili Fossae region by Brown et al. (2010), though it should be noted that saponite was also detected there. Nili Fossae is adjacent to the Isidis impact basin that has an extremely thin crust in its interior and upper mantle materials could have been excavated there by this impact event (Wieczorek et al., 2022). Thus, even though some differences in the observed alteration products exist, the carbonated serpentine at Nili Fossae could potentially be representative of local alteration of upper mantle materials at extremely high water-to-rock ratios.

The alteration of pyroxenite at low water-to-rock ratios produces serpentine, saponite, secondary pyroxene, and minor chlorite (<5 wt%). Increasing the water-to-rock ratio to 10 increases the amounts of all the hydrated/hydroxylated minerals and further leads to the formation of small quantities of carbonates (about 2 wt%). This mineral assemblage better represents most of the serpentine-rich outcrops that have been described on Mars (e.g., Brown et al., 2010). Interestingly, this assemblage also matches some of the alteration products reported in nakhlites when serpentine is present (Changela & Bridges, 2010). Thus, hydrous alteration of a pyroxenite protolith could potentially account for much of the hydrous alteration products found on Mars. For high water-to-rock ratios typical of a system dominated by the fluid chemistry, carbonate is the main alteration product followed by nontronite, talc, chlorite and oxides (hematite and magnetite). When reported on Mars, carbonates are always present in a mixture with phyllosilicates and these phyllosilicates are mainly saponite or nontronite (Bridges

et al., 2019). We thus consider such detections of carbonates and phyllosilicates as being potentially a result of CO<sub>2</sub>-rich aqueous processes that affected locally the crust of Mars. We note that such a high water-to-rock ratio is unlikely to occur in a hydrothermal system inside the crust along fractures, and that this would instead require a large aquifer or standing bodies of water along with long interaction times (>10,000 of years).

Finally, the alteration products of shergottite protoliths at low water-to-rock ratios are secondary pyroxene, saponite, serpentine, and chlorite. At intermediate water-to-rock ratios, the same assemblage is predicted but with the addition of talc. These mineral assemblages are comparable to those on Mars where serpentine has been detected, but also where altered crust has been detected without serpentine, such as in the southern highlands (e.g., Bultel et al., 2015) or in altered crust excavated by impact craters (e.g., Sun & Milliken, 2014). Interestingly, strong magnetic anomalies are found between the Hellas and Isidis impact basins where serpentine was detected. Alteration of a shergottite protolith at low to moderate water-to-rock ratios could thus explain many observed hydrous mineral assemblages on Mars. In the case of higher water-to-rock ratios, we obtained similar mineral assemblages as with the alteration of pyroxenite protoliths (mainly carbonates). This is because the reaction is mainly controlled by the composition of the fluid. As for pyroxenite alteration at extremely high water-to-rock ratios, we consider this to be potentially representative of some hydrothermally altered crust on Mars.

## 6. Conclusions

Mars at one point in its past was able to sustain a core generated dynamo and thus a global magnetic field. Portions of the crust were magnetized during this time, and the present day lithospheric magnetic anomalies on Mars are strong in comparison to those on Earth. The origin of these anomalies has long been debated. The magnetic minerals responsible for crustal magnetization are not known with certainty, though magnetite and pyrrhotite are the most likely candidates (e.g., Dunlop & Arkani-Hamed, 2005). Further, magnetization acquisition processes are also uncertain, and primary magmatic processes, aqueous alteration, and impact processes all could have played a role. The depth and thickness of magnetic sources are notoriously difficult to constrain from orbital magnetic field data alone, though the sources are probably shallower in the northern lowlands than in the southern highlands (e.g., Gong & Wieczorek, 2021). Lastly, the strength of the magnetizing field is poorly constrained, and is based on only a single Martian meteorite (Weiss et al., 2008).

In this study, we first derived a lower bound on the magnetization that is required to account for the strongest magnetic field strengths measured from the orbit and the magnetic field strength measured at the InSight lander. Our model employed a geologically plausible compact magnetic source that is unidirectionally magnetized, and the depth and thickness of the magnetic source were constrained from crustal models based on InSight seismic data. The abundance of magnetite required to account for these magnetizations was determined by assuming an Earth-like ambient magnetic field when the magnetic minerals formed. Assuming a magnetic layer thickness between 10 and 40 km, we found that between 2 and 7 wt% magnetite was required to account for the strongest orbital magnetic field strengths. In contrast, only 0.4 to 1 wt% magnetite was required to account for the measured field strengths at the InSight lander when the magnetization was confined to one or more of the three major crustal layers imaged by the InSight seismometer.

We next investigated whether the aqueous alteration of known Martian rock types could generate the required abundances of magnetite. In almost all cases, the only magnetic mineral that was generated was magnetite. When considering low water-to-rock ratios, the only investigated protolith that could account for the strongest orbital magnetic fields was dunite. Between 1 and 6 wt% magnetite could be generated when considering a range of olivine compositions and alteration temperatures. While serpentinization of dunite is a possible origin for the strongest magnetic anomalies, accounting for an equivalent layer of dunite that is more than 10 km thick is geologically problematic. In this regard, we note that the aqueous alteration of dunite generates mostly serpentine with only low abundances of other clay minerals, which is not consistent with the mineralogy of the serpentine deposits found on Mars. Nevertheless, dunitic source rocks on Mars are likely to form deep in the crust, and would only be found rarely at the surface when excavated by large impact craters.

When the water-to-rock ratio was increased to 10, we found that the alteration of pyroxenites and shergottites could generate up to 0.3 and 0.4 wt% magnetite, respectively. These abundances could account for the measured magnetic field strength at the InSight lander if the magnetization is confined to one or more of the three major crustal layers detected by InSight. For both protoliths, the alteration products include serpentine, saponite, chlorite, and carbonates, which are usually found at serpentine outcrops on Mars. Thus, the hydrous alteration of

pyroxenites or basaltic shergottites is a plausible origin for many of the moderate strength magnetic anomalies on Mars. Altering these protoliths at even higher water-to-rock ratios of 100 or 1000 can generate even more magnetite (up to 4 wt%), but such water-to-rock ratios are probably unrealistically high when considering magnetic sources that are 10–100s of km in size.

## Data Availability Statement

Version 8.0a of EQ3/6 developed by Tom Wolery at Lawrence Livermore National Laboratory is available at Wolery (2010). The input parameters allowing to reproduce our work and outputs are available in Supporting Information S1.

## Acknowledgments

The French authors acknowledge the French Space Agency (CNES) and the French National Research Agency (ANR-14-CE36-0012-02 and ANR-19-CE31-0008-08) for funding the InSight science analysis. Benjamin Bultel was also partly supported by the “Institut National des Sciences de l’Univers” (INSU), the “Centre National de la Recherche Scientifique” (CNRS), and the “Centre National d’Etude Spatiales” (CNES) through the “Programme National de la Planétologie.” AM acknowledges funding from the Harvard Daly Fellowship and SNF Ambizione (PZ00P2\_209123). CLJ acknowledges support from the InSight Mission (JPL) during the early stages of this work, and from the Natural Sciences and Engineering Research Council of Canada. We acknowledge the following institutions for the loan of Martian meteorite samples: University of Washington (Seattle, USA), University of New Mexico (Albuquerque, USA), Museum für Naturkunde (Berlin Germany). We thank the two anonymous reviewers as well as the Editor Laurent Montési for their careful reading and their insightful comments and suggestions that greatly improved our manuscript.

## References

- Acuña, M. H., Connerney, J. E. P., Ness, N. F., Lin, R. P., Mitchell, D., Carlson, C. W., et al. (1999). Global distribution of crustal magnetization discovered by the Mars global surveyor MAG/ER experiment. *Science*, *284*(5415), 790–793. <https://doi.org/10.1126/science.284.5415.790>
- Agee, C. B., Wilson, N. V., McCubbin, F. M., Ziegler, K., Polyak, V. J., Sharp, Z. D., et al. (2013). Unique meteorite from early Amazonian Mars: Water-rich basaltic breccia Northwest Africa 7034. *Science*, *339*(6121), 780–785. <https://doi.org/10.1126/science.1228858>
- Amador, E. S., Bandfield, J. L., & Thomas, N. H. (2018). A search for minerals associated with serpentinization across Mars using CRISM spectral data. *Icarus*, *311*, 113–134. <https://doi.org/10.1016/j.icarus.2018.03.021>
- Barshad, I. (1948). Vermiculite and its relation to biotite as revealed by base exchange reactions, X-ray analyses, differential thermal curves, and water content. *American Mineralogist: Journal of Earth and Planetary Materials*, *33*(11–12), 655–678.
- Bellucci, J. J., Nemchin, A. A., Whitehouse, M. J., Humayun, M., Hewins, R., & Zanda, B. (2015). Pb-isotopic evidence for an early, enriched crust on Mars. *Earth and Planetary Science Letters*, *410*, 34–41. <https://doi.org/10.1016/j.epsl.2014.11.018>
- Berger, J. A., Schmidt, M. E., Gellert, R., Boyd, N. I., Desouza, E. D., Flemming, R. L., et al. (2017). Zinc and germanium in the sedimentary rocks of Gale Crater on Mars indicate hydrothermal enrichment followed by diagenetic fractionation. *Journal of Geophysical Research: Planets*, *122*(8), 1747–1772. <https://doi.org/10.1002/2017je005290>
- Bishop, J. L., Tirsch, D., Tornabene, L. L., Jaumann, R., McEwen, A. S., McGuire, P. C., et al. (2013). Mineralogy and morphology of geologic units at Libya Montes, Mars: Ancient aqueously derived outcrops, mafic flows, fluvial features, and impacts. *Journal of Geophysical Research: Planets*, *118*(3), 487–513. <https://doi.org/10.1029/2012je004151>
- Bouvier, L. C., Costa, M. M., Connelly, J. N., Jensen, N. K., Wielandt, D., Storey, M., et al. (2018). Evidence for extremely rapid magma ocean crystallization and crust formation on Mars. *Nature*, *558*(7711), 586–589. <https://doi.org/10.1038/s41586-018-0222-z>
- Bridges, J. C., Hicks, L. J., & Treiman, A. H. (2019). Carbonates on Mars. In *Volatiles in the Martian crust* (pp. 89–118). Elsevier.
- Bridges, J. C., & Schwenzer, S. P. (2012). The nakhlite hydrothermal brine on Mars. *Earth and Planetary Science Letters*, *359*, 117–123. <https://doi.org/10.1016/j.epsl.2012.09.044>
- Bristow, T. F., Bish, D. L., Vaniman, D. T., Morris, R. V., Blake, D. F., Grotzinger, J. P., et al. (2015). The origin and implications of clay minerals from Yellowknife Bay, Gale crater, Mars. *American Mineralogist*, *100*(4), 824–836. <https://doi.org/10.2138/am-2015-5077ccbyncnd>
- Bristow, T. F., Rampe, E. B., Achilles, C. N., Blake, D. F., Chipera, S. J., Craig, P., et al. (2018). Clay mineral diversity and abundance in sedimentary rocks of Gale crater, Mars. *Science Advances*, *4*(6), eaar3330. <https://doi.org/10.1126/sciadv.aar3330>
- Brown, A. J., Hook, S. J., Baldrige, A. M., Crowley, J. K., Bridges, N. T., Thomson, B. J., et al. (2010). Hydrothermal formation of clay-carbonate alteration assemblages in the Nili Fossae region of Mars. *Earth and Planetary Science Letters*, *297*(1–2), 174–182. <https://doi.org/10.1016/j.epsl.2010.06.018>
- Bultel, B. (2024). Aqueous alteration as an origin of Martian magnetization [Dataset]. *Zenodo*. <https://doi.org/10.5281/zenodo.12784397>
- Bultel, B., Quantin-Nataf, C., Andréani, M., Clénet, H., & Lozac’h, L. (2015). Deep alteration between Hellas and Isidis basins. *Icarus*, *260*, 141–160. <https://doi.org/10.1016/j.icarus.2015.06.037>
- Butler, R. F. (1998). *Paleomagnetism: Magnetic domains to geologic terranes*. Blackwell.
- Carter, J., Poulet, F., Bibring, J. P., Mangold, N., & Murchie, S. (2013). Hydrous minerals on Mars as seen by the CRISM and OMEGA imaging spectrometers: Updated global view. *Journal of Geophysical Research: Planets*, *118*(4), 831–858. <https://doi.org/10.1029/2012je004145>
- Catling, D. C. (1999). A chemical model for evaporites on early Mars: Possible sedimentary tracers of the early climate and implications for exploration. *Journal of Geophysical Research*, *104*(E7), 16453–16469. <https://doi.org/10.1029/1998je001020>
- Changela, H. G., & Bridges, J. C. (2010). Alteration assemblages in the nakhlites: Variation with depth on Mars. *Meteoritics & Planetary Sciences*, *45*(12), 1847–1867. <https://doi.org/10.1111/j.1945-5100.2010.01123.x>
- Chassefière, E., Langlais, B., Quesnel, Y., & Leblanc, F. (2013). The fate of early Mars’ lost water: The role of serpentinization. *Journal of Geophysical Research: Planets*, *118*(5), 1123–1134. <https://doi.org/10.1002/jgre.20089>
- Chassefière, E., & Leblanc, F. (2011). Constraining methane release due to serpentinization by the observed D/H ratio on Mars. *Earth and Planetary Science Letters*, *310*(3–4), 262–271. <https://doi.org/10.1016/j.epsl.2011.08.013>
- Connerney, J. E. P. (2015). 10.06—Planetary magnetism. In G. Schubert (Ed.), *Treatise on geophysics* (2nd ed., pp. 195–237). Elsevier. <https://doi.org/10.1016/B978-0-444-53802-4.00171-8>
- Dunlop, D. J., & Arkani-Hamed, J. (2005). Magnetic minerals in the Martian crust. *Journal of Geophysical Research*, *110*(E12), E12S04. <https://doi.org/10.1029/2005JE002404>
- Dunlop, D. J., & Özdemir, Ö. (1997). In D. Edwards (Ed.), *Rock magnetism: Fundamentals and frontiers* (p. 573). Cambridge University Press.
- Dunlop, D. J., & Özdemir, Ö. (2015). Magnetizations in rocks and minerals. In G. Schubert (Ed.), *Treatise on geophysics* (2nd ed.) (Vol. 5, pp. 255–308). Elsevier. <https://doi.org/10.1016/B978-0-444-53802-4.00102-0>
- Ehlmann, B. L., Mustard, J. F., & Murchie, S. L. (2010). Geologic setting of serpentine deposits on Mars. *Geophysical Research Letters*, *37*(6), L06201. <https://doi.org/10.1029/2010gl042596>
- Evans, B. W. (2008). Control of the products of serpentinization by the Fe<sup>2+</sup>–Mg–1 exchange potential of olivine and orthopyroxene. *Journal of Petrology*, *49*(10), 1873–1887. <https://doi.org/10.1093/ptrology/egn050>
- Gattacceca, J., Rochette, P., Scorzelli, R. B., Munayco, P., Agee, C., Quesnel, Y., et al. (2014). Martian meteorites and Martian magnetic anomalies: A new perspective from NWA 7034: Martian meteorites & magnetic anomalies. *Geophysical Research Letters*, *41*(14), 4859–4864. <https://doi.org/10.1002/2014GL060464>



- Gong, S., & Wiczcerek, M. (2021). Depth of Martian magnetization from localized power spectrum analysis. *Journal of Geophysical Research: Planets*, 126(8), e2020JE006690. <https://doi.org/10.1029/2020JE006690>
- Griffith, L. L., & Shock, E. L. (1995). A geochemical model for the formation of hydrothermal carbonates on Mars. *Nature*, 377(6548), 406–408. <https://doi.org/10.1038/377406a0>
- Griffith, L. L., & Shock, E. L. (1997). Hydrothermal hydration of Martian crust: Illustration via geochemical model calculations. *Journal of Geophysical Research*, 102(E4), 9135–9143. <https://doi.org/10.1029/96je02939>
- Harrison, K. P., & Grimm, R. E. (2002). Controls on Martian hydrothermal systems: Application to valley network and magnetic anomaly formation. *Journal of Geophysical Research*, 107(E5), e2023JE007779. <https://doi.org/10.1029/2023JE007779>
- Hauk, S. A., & Phillips, R. J. (2002). Thermal and crustal evolution of Mars. *Journal of Geophysical Research*, 107(E7), 1–19. <https://doi.org/10.1029/2001JE001801>
- Herd, C. D. K., Walton, E. L., Agee, C. B., Muttik, N., Ziegler, K., Shearer, C. K., et al. (2017). The Northwest Africa 8159 martian meteorite: Expanding the martian sample suite to the early Amazonian. *Geochimica et Cosmochimica Acta*, 218, 1–26. <https://doi.org/10.1016/j.gca.2017.08.037>
- Hicks, L. J., Bridges, J. C., & Gurman, S. J. (2014). Ferric saponite and serpentine in the nakhlite martian meteorites. *Geochimica et Cosmochimica Acta*, 136, 194–210. <https://doi.org/10.1016/j.gca.2014.04.010>
- Humayun, M., Nemchin, A., Zanda, B., Hewins, R. H., Grange, M., Kennedy, A., et al. (2013). Origin and age of the earliest Martian crust from meteorite NWA 7533. *Nature*, 503(7477), 513–516. <https://doi.org/10.1038/nature12764>
- Ikedai, Y. (1994). Petrography and petrology of the ALH-77005 shergottite. *Antarctic Meteorite Research*, 7, 9.
- Johnson, C. L., Mittelholz, A., Langlais, B., Russell, C. T., Ansan, V., Banfield, D., et al. (2020). Crustal and time-varying magnetic fields at the InSight landing site on Mars. *Nature Geoscience*, 13(3), 199–204. <https://doi.org/10.1038/s41561-020-0537-x>
- Khan, A., Sossi, P. A., Liebske, C., Rivoldini, A., & Giardini, D. (2022). Geophysical and cosmochemical evidence for a volatile-rich Mars. *Earth and Planetary Science Letters*, 578, 117330. <https://doi.org/10.1016/j.epsl.2021.117330>
- Klein, F., Bach, W., Humphris, S. E., Kahl, W. A., Jöns, N., Moskowitz, B., & Berquó, T. S. (2014). Magnetite in seafloor serpentinite—Some like it hot. *Geology*, 42(2), 135–138. <https://doi.org/10.1130/g35068.1>
- Krämer Ruggiu, L., Gattacceca, J., Devouard, B., Udry, A., Debaille, V., Rochette, P., et al. (2020). Caleta el Cobre 022 Martian meteorite: Increasing nakhlite diversity. *Meteoritics & Planetary Sciences*, 55(7), 1539–1563. <https://doi.org/10.1111/maps.13534>
- Langlais, B., Lesur, V., Purucker, M. E., Connerney, J. E. P., & Mandea, M. (2010). Crustal magnetic fields of terrestrial planets. *Space Science Reviews*, 152(1–4), 223–249. <https://doi.org/10.1007/s11214-009-9557-y>
- Langlais, B., Thébaud, E., Houlié, A., Purucker, M. E., & Lillis, R. J. (2019). A new model of the crustal magnetic field of Mars using MGS and MAVEN. *Journal of Geophysical Research: Planets*, 124(6), 1542–1569. <https://doi.org/10.1029/2018JE005854>
- Lesur, V., & Vervelidou, F. (2019). Retrieving lithospheric magnetisation distribution from magnetic field models. *Geophysical Journal International*, ggz471. <https://doi.org/10.1093/gji/ggz471>
- Liu, Y., Tice, M. M., Schmidt, M. E., Treiman, A. H., Kizovski, T. V., Hurowitz, J. A., et al. (2022). An olivine cumulate outcrop on the floor of Jezero crater, Mars. *Science*, 377(6614), 1513–1519. <https://doi.org/10.1126/science.abo2756>
- Lognonné, P., Banerdt, W. B., Pike, W. T., Giardini, D., Christensen, U., Garcia, R. F., et al. (2020). Constraints on the shallow elastic and anelastic structure of Mars from InSight seismic data. *Nature Geoscience*, 13(3), 213–220. <https://doi.org/10.1038/s41561-020-0536-y>
- Lyons, J. R., Manning, C., & Nimmo, F. (2005). Formation of methane on Mars by fluid-rock interaction in the crust. *Geophysical Research Letters*, 32(13), L13201. <https://doi.org/10.1029/2004gl022161>
- Maurel, C., & Gattacceca, J. (2023). Estimating paleointensities from chemical remanent magnetizations of magnetite using non-heating methods. *Journal of Geophysical Research: Planets*, 128(6), e2023JE007779. <https://doi.org/10.1029/2023je007779>
- McAdam, A. C., Sutter, B., Archer, P. D., Franz, H. B., Wong, G. M., Lewis, J. M. T., et al. (2020). Constraints on the mineralogy and geochemistry of Vera Rubin ridge, Gale crater, Mars, from Mars Science Laboratory sample analysis at Mars evolved gas analyses. *Journal of Geophysical Research: Planets*, 125(11), e2019JE006309. <https://doi.org/10.1029/2019je006309>
- McCollom, T. M., Klein, F., Moskowitz, B., Berquó, T. S., Bach, W., & Templeton, A. S. (2020). Hydrogen generation and iron partitioning during experimental serpentinization of an olivine–pyroxene mixture. *Geochimica et Cosmochimica Acta*, 282, 55–75. <https://doi.org/10.1016/j.gca.2020.05.016>
- McCollom, T. M., Klein, F., & Ramba, M. (2022). Hydrogen generation from serpentinization of iron-rich olivine on Mars, icy moons, and other planetary bodies. *Icarus*, 372, 114754. <https://doi.org/10.1016/j.icarus.2021.114754>
- McCubbin, F. M., Boyce, J. W., Novák-Szabó, T., Santos, A. R., Tartèse, R., Muttik, N., et al. (2016). Geologic history of Martian regolith breccia Northwest Africa 7034: Evidence for hydrothermal activity and lithologic diversity in the Martian crust. *Journal of Geophysical Research: Planets*, 121(10), 2120–2149. <https://doi.org/10.1002/2016JE005143>
- McDonough, W. F., & Sun, S.-S. (1995). The composition of the Earth. *Chemical Geology*, 120(3–4), 223–253. [https://doi.org/10.1016/0009-2541\(94\)00140-4](https://doi.org/10.1016/0009-2541(94)00140-4)
- McSween, H. Y., & Lauretta, D. S. (2006). Meteorites and the early solar system II.
- McSween, H. Y., & McLennan, S. M. (2014). Mars. In H. D. Holland & K. K. Turekian (Eds.), *Treatise on geochemistry* (2nd ed., pp. 251–300). Elsevier. <https://doi.org/10.1016/B978-0-08-095975-7.00125-X>
- McSween, H. Y., Ruff, S. W., Morris, R. V., Gellert, R., Klingelhöfer, G., Christensen, P. R., et al. (2008). Mineralogy of volcanic rocks in Gusev crater, Mars: Reconciling Mössbauer, alpha particle X-ray spectrometer, and miniature thermal emission spectrometer spectra. *Journal of Geophysical Research*, 113(E6), E06S04. <https://doi.org/10.1029/2007je002970>
- Michalski, J. R., & Niles, P. B. (2010). Deep crustal carbonate rocks exposed by meteor impact on Mars. *Nature Geoscience*, 3(11), 751–755. <https://doi.org/10.1038/ngeo971>
- Mittelholz, A., Johnson, C. L., Fillingim, M., Grimm, R. E., Joy, S., Thorne, S. N., & Banerdt, W. B. (2023). Mars' external magnetic field as seen from the surface with InSight. *Journal of Geophysical Research: Planets*, 128(1), e2022JE007616. <https://doi.org/10.1029/2022je007616>
- Morris, R. V., Klingelhöfer, G., Schröder, C., Fleischer, I., Ming, D. W., Yen, A. S., et al. (2008). Iron mineralogy and aqueous alteration from Husband Hill through Home Plate at Gusev crater, Mars: Results from the Mössbauer instrument on the Spirit Mars exploration rover. *Journal of Geophysical Research*, 113, E12. <https://doi.org/10.1029/2008je003201>
- Morris, R. V., Rampe, E. B., Vaniman, D. T., Christoffersen, R., Yen, A. S., Morrison, S. M., et al. (2020). Hydrothermal precipitation of sanidine (adularia) having full Al, Si structural disorder and specular hematite at Maunakea volcano (Hawaii) and at Gale Crater (Mars). *Journal of Geophysical Research: Planets*, 125(9), e2019JE006324. <https://doi.org/10.1029/2019je006324>
- Morris, R. V., Vaniman, D. T., Blake, D. F., Gellert, R., Chipera, S. J., Rampe, E. B., et al. (2016). Silicic volcanism on Mars evidenced by tridymite in high-SiO<sub>2</sub> sedimentary rock at Gale crater. *Proceedings of the National Academy of Sciences*, 113(26), 7071–7076. <https://doi.org/10.1073/pnas.1607098113>



- Nyquist, L. E., Shih, C., McCubbin, F. M., Santos, A. R., Shearer, C. K., Peng, Z. X., et al. (2016). Rb-Sr and Sm-Nd isotopic and REE studies of igneous components in the bulk matrix domain of Martian breccia Northwest Africa 7034. *Meteoritics & Planetary Sciences*, 51(3), 483–498. <https://doi.org/10.1111/maps.12606>
- Ody, A., Poulet, F., Langevin, Y., Bibring, J., Bellucci, G., Altieri, F., et al. (2012). Global maps of anhydrous minerals at the surface of Mars from OMEGA/MEX. *Journal of Geophysical Research*, 117(E11), E00J14. <https://doi.org/10.1029/2012je004117>
- Oliveira, J. S., Wiczeorek, M. A., & Kletetschka, G. (2017). Iron abundances in lunar impact basin melt sheets from orbital magnetic field data. *Journal of Geophysical Research: Planets*, 122(12), 2429–2444. <https://doi.org/10.1002/2017JE005397>
- O'Reilly, W. (1984). Magnetic minerals in rocks. In W. O'Reilly (Ed.), *Rock and mineral magnetism* (pp. 7–29). Springer US. [https://doi.org/10.1007/978-1-4684-8468-7\\_2](https://doi.org/10.1007/978-1-4684-8468-7_2)
- Parker, R. L. (1991). A theory of ideal bodies for seamount magnetism. *Journal of Geophysical Research*, 96(B10), 16101–16112. <https://doi.org/10.1029/91JB01497>
- Parker, R. L. (2003). Ideal bodies for Mars magnetism. *Journal of Geophysical Research*, 108(E1), 5006. <https://doi.org/10.1029/2001JE001760>
- Quesnel, Y., Sotin, C., Langlais, B., Costin, S., Manda, M., Gottschalk, M., & Dymont, J. (2009). Serpentinization of the martian crust during Noachian. *Earth and Planetary Science Letters*, 277(1–2), 184–193. <https://doi.org/10.1016/j.epsl.2008.10.012>
- Ramirez, R. M., Craddock, R. A., & Usui, T. (2020). Climate simulations of early Mars with estimated precipitation, runoff, and erosion rates. *Journal of Geophysical Research: Planets*, 125(3), e2019JE006160. <https://doi.org/10.1029/2019je006160>
- Rampe, E. B., Blake, D. F., Bristow, T. F., Ming, D. W., Vaniman, D. T., Morris, R. V., et al. (2020). Mineralogy and geochemistry of sedimentary rocks and eolian sediments in Gale crater, Mars: A review after six Earth years of exploration with curiosity. *Geochemistry*, 80(2), 125605. <https://doi.org/10.1016/j.chemer.2020.125605>
- Rochette, P., Gattacceca, J., Chevrier, V., Hoffmann, V., Lorand, J.-P., Funaki, M., & Hochleitner, R. (2005). Matching Martian crustal magnetization and magnetic properties of Martian meteorites. *Meteoritics & Planetary Sciences*, 40(4), 529–540. <https://doi.org/10.1111/j.1945-5100.2005.tb00961.x>
- Santos, A. R., Agee, C. B., McCubbin, F. M., Shearer, C. K., Burger, P. V., Tartèse, R., & Anand, M. (2015). Petrology of igneous clasts in Northwest Africa 7034: Implications for the petrologic diversity of the martian crust. *Geochimica et Cosmochimica Acta*, 157, 56–85. <https://doi.org/10.1016/j.gca.2015.02.023>
- Sautter, V., Toplis, M. J., Wiens, R. C., Cousin, A., Fabre, C., Gasnault, O., et al. (2015). In situ evidence for the continental crust on early Mars. *Nature Geoscience*, 8(8), 605–609. <https://doi.org/10.1038/ngeo2474>
- Schwenzer, S. P., & Kring, D. A. (2009). Impact-generated hydrothermal systems capable of forming phyllosilicates on Noachian Mars. *Geology*, 37(12), 1091–1094. <https://doi.org/10.1130/g30340a.1>
- Semprich, J., Filiberto, J., Treiman, A. H., & Schwenzer, S. P. (2022). Constraints on the formation of carbonates and low-grade metamorphic phases in the Martian crust as a function of H<sub>2</sub>O-CO<sub>2</sub> fluids. *Meteoritics & Planetary Sciences*, 57(1), 77–104. <https://doi.org/10.1111/maps.13775>
- Seyfried, W., & Bischoff, J. L. (1977). Hydrothermal transport of heavy metals by seawater: The role of seawater/basalt ratio. *Earth and Planetary Science Letters*, 34(1), 71–77. [https://doi.org/10.1016/0012-821x\(77\)90107-8](https://doi.org/10.1016/0012-821x(77)90107-8)
- Seyfried Jr, W. E., & Bischoff, J. L. (1979). Low temperature basalt alteration by sea water: An experimental study at 70 C and 150 C. *Geochimica et Cosmochimica Acta*, 43(12), 1937–1947. [https://doi.org/10.1016/0016-7037\(79\)90006-1](https://doi.org/10.1016/0016-7037(79)90006-1)
- Seyfried Jr, W. E., & Bischoff, J. L. (1981). Experimental seawater-basalt interaction at 300 C, 500 bars, chemical exchange, secondary mineral formation and implications for the transport of heavy metals. *Geochimica et Cosmochimica Acta*, 45(2), 135–147. [https://doi.org/10.1016/0016-7037\(81\)90157-5](https://doi.org/10.1016/0016-7037(81)90157-5)
- Smrekar, S. E., Lognonné, P., Spohn, T., Banerdt, W. B., Breuer, D., Christensen, U., et al. (2019). Pre-mission InSights on the interior of Mars. *Space Science Reviews*, 215, 1–72. <https://doi.org/10.1007/s11214-018-0563-9>
- Sun, V. Z., & Milliken, R. E. (2014). The geology and mineralogy of Richey crater, Mars: Evidence for post-Noachian clay formation. *Journal of Geophysical Research: Planets*, 119(4), 810–836. <https://doi.org/10.1002/2013je004602>
- Thébault, E., Hulot, G., Langlais, B., & Vigneron, P. (2021). A spherical harmonic model of Earth's lithospheric magnetic field up to degree 1050. *Geophysical Research Letters*, 48(21), e2021GL095147. <https://doi.org/10.1029/2021GL095147>
- Treiman, A. H. (2005). The nakhlite meteorites: Augite-rich igneous rocks from Mars. *Geochemistry*, 65(3), 203–270. <https://doi.org/10.1016/j.chemer.2005.01.004>
- Turbet, M. (2018). Habitability of planets using numerical climate models. Application to extrasolar planets and early Mars (Doctoral dissertation, Sorbonne Université).
- Udry, A., Howarth, G. H., Herd, C. D. K., Day, J. M. D., Lapen, T. J., & Filiberto, J. (2020). What Martian meteorites reveal about the interior and surface of Mars. *Journal of Geophysical Research: Planets*, 125(12), e2020JE006523. <https://doi.org/10.1029/2020JE006523>
- Viennet, J. C., Bultel, B., Riu, L., & Werner, S. C. (2017). Dioctahedral phyllosilicates versus zeolites and carbonates versus zeolites competitions as constraints to understanding early Mars alteration conditions. *Journal of Geophysical Research: Planets*, 122(11), 2328–2343. <https://doi.org/10.1002/2017je005343>
- Wänke, H., & Dreibus, G. (1994). Chemistry and accretion history of Mars. *Philosophical Transactions of the Royal Society of London*, A349, 285–293.
- Warner, N. H., Golombek, M. P., Ansan, V., Marteau, E., Williams, N., Grant, J. A., et al. (2022). In situ and orbital stratigraphic characterization of the InSight landing site-A type example of a regolith? Covered Lava Plain on Mars. *Journal of Geophysical Research: Planets*, 127(4), e2022JE007232. <https://doi.org/10.1029/2022JE007232>
- Weiss, B. P., Fong, L. E., Vali, H., Lima, E. A., & Baudenbacher, F. J. (2008). Paleointensity of the ancient Martian magnetic field. *Geophysical Research Letters*, 35(23), L23207. <https://doi.org/10.1029/2008GL035585>
- Weiss, B. P., & Tikoo, S. M. (2014). The lunar dynamo. *Science*, 346(6214), 1246753. <https://doi.org/10.1126/science.1246753>
- Wiczeorek, M. A. (2018). Strength, depth, and geometry of magnetic sources in the crust of the moon from localized power spectrum analysis. *Journal of Geophysical Research: Planets*, 123(1), 291–316. <https://doi.org/10.1002/2017JE005418>
- Wiczeorek, M. A., Broquet, A., McLennan, S. M., Rivoldini, A., Golombek, M., Antonangeli, D., et al. (2022). InSight constraints on the global character of the Martian Crust. *Journal of Geophysical Research: Planets*, 127(5), e2022JE007298. <https://doi.org/10.1029/2022JE007298>
- Wiczeorek, M. A., Weiss, B. P., & Stewart, S. T. (2012). An impactor origin for lunar magnetic anomalies. *Science*, 335(6073), 1212–1215. <https://doi.org/10.1126/science.1214773>
- Wolery, T. J. (2010). *EQ3/6 A software package for geochemical modeling (No. EQ3/6 V. 8.0 a)*. Lawrence Livermore National Laboratory (LLNL).
- Wolery, T. J., Jackson, K. J., Bourcier, W. L., Bruton, C. J., Viani, B. E., Knauss, K. G., & Delany, J. M. (1990). Current status of the EQ3/6 software package for geochemical modeling. *ACS Symposium Series*, 104–116. <https://doi.org/10.1021/bk-1990-0416.ch008>

- Wolery, T. W., & Jarek, R. L. (2003). Software user's manual. EQ3/6, version, 8, 376. Wolery, T. J. EQ3/6 A software package for geochemical modeling. Computer Software. <https://doi.org/10.11578/dc.20210416.44>
- Yen, A. S., Morris, R. V., Ming, D. W., Schwenzer, S. P., Sutter, B., Vaniman, D. T., et al. (2021). Formation of tridymite and evidence for a hydrothermal history at gale crater, Mars. *Journal of Geophysical Research: Planets*, 126(3), e2020JE006569. <https://doi.org/10.1029/2020je006569>
- Yoshizaki, T., & McDonough, W. F. (2020). The composition of Mars. *Geochimica et Cosmochimica Acta*, 273, 137–162. <https://doi.org/10.1016/j.gca.2020.01.011>
- Zolotov, M. Y. (2007). An oceanic composition on early and today's Enceladus. *Geophysical Research Letters*, 34(23), L23203. <https://doi.org/10.1029/2007gl031234>
- Zolotov, M. Y. (2012). Aqueous fluid composition in CI chondritic materials: Chemical equilibrium assessments in closed systems. *Icarus*, 220(2), 713–729. <https://doi.org/10.1016/j.icarus.2012.05.036>

### References From the Supporting Information

- Herd, C. D. K. (2023). Insights into the petrogenetic history of the Northwest Africa 7635 augite-rich shergottite. *Meteoritics & Planetary Sciences*, 58(1), 158–164. <https://doi.org/10.1111/maps.13935>
- Van de Moortèle, B., Reynard, B., Rochette, P., Jackson, M., Beck, P., Gillet, P., et al. (2007). Shock-induced metallic iron nanoparticles in olivine-rich Martian meteorites. *Earth and Planetary Science Letters*, 262(1–2), 37–49. <https://doi.org/10.1016/j.epsl.2007.07.002>
- Warr, L. N. (2021). IMA–CNMNC approved mineral symbols. *Mineralogical Magazine*, 85, 291–320. <https://doi.org/10.1180/mgm.2021.43>